

1 Easterly waves in the East Pacific during the OTREC 2019 field campaign

2 Lidia Huaman*

3 *Texas A&M University, Department of Atmospheric Sciences, College Station, Texas*

4 Eric D. Maloney

5 *Colorado State University, Department of Atmospheric Science, Fort Collins, Colorado*

6 Courtney Schumacher

7 *Texas A&M University, Department of Atmospheric Sciences, College Station, Texas*

8 George N. Kiladis

Physical Sciences Division, NOAA/Earth System Research Laboratory, Boulder, Colorado

¹⁰ *Corresponding author address: Lidia Huaman, Texas A&M University, Department of Atmospheric Sciences College Station, Texas

¹² E-mail: lidiana.huaman@tamu.edu

ABSTRACT

13 Easterly waves (EWs) are off-equatorial **tropical** synoptic disturbances with
14 a westward phase speed between $11\text{-}14 \text{ m s}^{-1}$. Over the East Pacific in boreal
15 summer, the combination of EWs and other synoptic disturbances, plus local
16 mechanisms **associated with** sea surface temperature (SST) gradients, define
17 the climatological structure of the Intertropical Convergence Zone (ITCZ).
18 The East Pacific ITCZ has both deep and shallow convection that is linked to
19 deep and shallow meridional circulations, respectively. The deep convection
20 is located around 9°N over warm SSTs. The shallow convection is located
21 around 6°N and is driven by the meridional SST gradient south of the ITCZ.
22 This study aims to document the interaction between east Pacific EWs and the
23 deep and shallow meridional circulations during the Organization of Tropical
24 East Pacific Convection (OTREC) field campaign in 2019 using field cam-
25 paign observations, ERA5 reanalysis, and satellite precipitation. We identi-
26 fied three EWs during the OTREC period using precipitation and dynamical
27 fields. Composite **analysis shows that the** convectively active part of the EW
28 enhances the ITCZ deep circulation and is associated with an export of col-
29 umn integrated moist static energy (MSE) by vertical advection. The sub-
30 sequent convectively suppressed, anticyclonic part of the EW enhances the
31 shallow circulation and the shallow overturning flow at 850 hPa. Horizontal
32 moisture advection associated with the EWs' anticyclonic circulation supports
33 **stronger and slightly deeper** shallow convection over the southern part of the
34 ITCZ and associated column integrated MSE import by vertical advection.
35 **Therefore, EWs appear to strongly modulate shallow and deep circulations in**
36 **the East Pacific ITCZ.**

37 **1. Introduction**

38 Easterly waves (EWs) are prominent synoptic (i.e., 2 to 10 day period) features in the Pacific
39 Intertropical Convergence Zone (ITCZ) with westward phase speeds between 11 - 14 m s⁻¹ (Serra
40 et al. 2008). **EWs commonly serve as precursors to tropical cyclones and hurricanes in the East**
41 **Pacific (Pasch et al. 2009; Serra et al. 2010) and** are associated with 25 to 40% of the deep con-
42 vective clouds and produce up to 50% of the seasonal precipitation over the far East Pacific during
43 boreal summer (Dominguez et al. 2020). **Thus, EWs impact both the weather and climate of the**
44 **East Pacific ITCZ.**

45 EWs are found in the Caribbean Sea (Riehl 1954), the western and central Pacific (Reed and
46 Recker 1971; Reed and Johnson 1974), the eastern Atlantic and West Africa (Reed et al. 1977; Ki-
47 ladis et al. 2006; Berry et al. 2007; Janiga and Thorncroft 2013; Gomes et al. 2019), and the East
48 Pacific (Tai and Ogura 1987; Raymond et al. 1998; Zehnder et al. 1999; Serra et al. 2008; Rydbeck
49 et al. 2017). In the East Pacific, EWs are consistent with Riehl's classical "inverted trough" model
50 (Riehl 1954). In this model, positive specific humidity anomalies are concentrated in the lower
51 troposphere in advance of the trough axis and deepen within and behind the trough where en-
52 hanced convection and column-integrated moisture anomalies are favored. The maximum vertical
53 component of vorticity is located **between 700 and 600 hPa and EW wavelengths range between**
54 **4200 and 5900 km**. Ahead of the wave (i.e., **west of the trough axis**), the planetary boundary layer
55 (PBL) is warm and moist, and northerly winds are predominant. Behind the wave (i.e., **east of**
56 **the trough axis**), the PBL is cold and dry and dominated by southerly winds. Serra et al. (2010)
57 showed that while some East Pacific EWs originate from Atlantic disturbances east of 70°W, oth-
58 ers are generated locally in the Caribbean and East Pacific. **Additionally, it is important to mention**
59 **that the EWs predominate over warm SST regions and notable mean meridional humidity gradi-**

60 ents. Rydbeck and Maloney (2015) showed that anomalous meridional winds acting on the mean
61 meridional moisture gradient of the ITCZ produce moisture anomalies that enhance convection in
62 the though side of the EW. The orientation of EWs is generally southwest-northeast, which helps
63 an EW maintain kinetic energy through barotropic conversion in the presence of a meridionally
64 sheared zonal flow (Rydbeck and Maloney 2014; Rennick 1976; Thorncroft and Hoskins 1994).

65 EWs are important features of the East Pacific ITCZ. The net effect of many synoptic-scale
66 disturbances, such as EWs and convectively coupled equatorial waves (CCEWs; Kiladis et al.
67 2009; Serra et al. 2014; Huaman et al. 2020), plus local mechanisms like low-level convergence
68 produced by strong meridional sea surface temperature (SST) gradients (Lindzen and Nigam 1987;
69 Back and Bretherton 2009), define the climatological structure of the ITCZ. The **mean** vertical
70 structure of the East Pacific ITCZ has been studied in some detail. Back and Bretherton (2006)
71 showed maximum vertical motion at 850 hPa based on reanalysis fields **that was associated with**
72 **an import of moist static energy (MSE) through vertical advection.** However, a second vertical
73 motion peak aloft was observed using **two** months of data from the East Pacific Investigation of
74 Climate Processes in the Coupled Ocean – Atmosphere System (EPIC-2001) field campaign and
75 satellite data (Zhang et al. 2004, 2008; Huaman and Takahashi 2016). Additionally, Huaman and
76 Schumacher (2018) used 16 years of CloudSat and Tropical Rainfall Measuring Mission (TRMM)
77 satellite data to demonstrate that two peaks of latent heating associated with deep and shallow
78 convection are apparent in this region and linked to deep and shallow **meridional** circulations.
79 They also found that the **vertical structure of the ITCZ** is tilted **meridionally; shallow convection**
80 **occurs around 6°N in the southern part of the ITCZ, and transitions to** deep convection around 9°N
81 in the northern part of the ITCZ .

82 Most of the studies in the East Pacific have relied on reanalyses to describe the three-dimensional
83 structure of EWs. The lack of direct observations in the East Pacific causes reanalysis datasets to

84 rely **heavily** on model physical parameterizations, supporting the need for targeted field cam-
85 paigns. Serra and Houze (2002) used the Tropical Eastern Pacific Process Study (TEPPS-1997)
86 research cruise dataset to study synoptic-scale convection and found that EWs are prominent con-
87 vective features during boreal summer. Petersen et al. (2003) used the EPIC-2001 field campaign
88 dataset to study EWs, revealing their thermodynamic characteristics and four-dimensional pre-
89 cipitation structure using shipborne C-band, Doppler radar data. The Organization of Tropical
90 East Pacific Convection (OTREC) is the latest field campaign over the East Pacific and took place
91 from 4 August to 2 October 2019 (Fuchs-Stone et al. 2020). OTREC goals were to determine
92 the large-scale environmental factors that control convection over the tropical oceans and to char-
93 acterize the interaction of convection with tropical disturbances, especially EWs. OTREC used
94 the NSF/NCAR Gulfstream V aircraft to survey the East Pacific and deploy gridded patterns of
95 dropsondes from a high altitude (i.e., 13 km) to characterize the large-scale environmental state
96 and integrated effects of convection. The aircraft also provided profiles of radar reflectivity with a
97 W-band radar.

98 Figure 1 shows the mean precipitation from the **Integrated Multi-satellitE Retrievals for Global**
99 **Precipitation Measurement (IMERG) dataset** and mean SST from the Operational Sea Surface
100 Temperature and Sea Ice Analysis (OSTIA) (left panel) and a cross section of vertical motion
101 and flow in the meridional plane over the far East Pacific from ERA5 reanalysis (right panel)
102 for August-September 2019, a period approximately corresponding to the OTREC field campaign
103 period. Section 2 describes the precipitation and reanalysis data sets in more detail. The OTREC
104 field campaign was held in the far East Pacific in a box delineated approximately by 89° - 86° W and
105 0° - 13° N (indicated by the blue rectangle in Fig. 1a); this will **hereafter** be called the OTREC region
106 box. Over the OTREC region box the maximum precipitation (Fig. 1a) was located around 9° N
107 over a weak SST gradient (i.e., the East Pacific warm pool) and precipitation extended towards

108 this region from the Colombian coast (Toma and Webster 2010a,b). A strong meridional SST
109 gradient was seen south of the precipitation maximum, with coldest SSTs south of the equator
110 (i.e., the East Pacific cold tongue). The vertical motion cross section (Fig. 1b) shows shallow
111 and deep vertical motion peaks associated with differing convective **profiles that are** linked to
112 shallow and deep circulations, respectively. Jaramillo et al. (2017) showed that the deep convection
113 located around 8°N over warmer SSTs is associated with mesoscale convective systems (MCSs),
114 while the shallow vertical motion peak at 6°N has been shown to be driven by the strong SST
115 meridional gradient and associated low-level convergence (Lindzen and Nigam 1987) that forms
116 shallow cloud structures with light precipitation (Huaman and Schumacher 2018). **The shallow**
117 **structures likely do not evolve into deep structures because of the cooler SST and dry upper-level**
118 **air in that region (Zuidema et al. 2006).**

119 Most previous studies about the vertical structure of the East Pacific ITCZ and associated cir-
120 culations have been focused on seasonal scales, but synoptic variations of the deep and shallow
121 circulations have not yet been examined in detail. Further, previous analyses were limited to re-
122 analysis data and satellite retrievals (e.g., Back and Bretherton 2006; Handlos and Back 2014;
123 Huaman and Takahashi 2016; Huaman and Schumacher 2018) because of the lack of observations
124 in the East Pacific. In this study, we aim to 1) characterize the synoptic variability in the East
125 Pacific during the OTREC 2019 field campaign, providing useful large-scale context for more
126 specialized studies in this region, and 2) understand how this synoptic variability influences con-
127 vection and deep and shallow circulations in the East Pacific ITCZ during OTREC by modulating
128 the moisture and MSE fields. The modulation of shallow and deep meridional circulations **associ-**
129 **ated with the** **passage of EWs will be assessed using ERA5 reanalysis fields**, satellite precipitation,
130 and OTREC field campaign data. Thompson et al. (1979) stated that shallow clouds were found
131 to be abundant near the EW ridge, whereas detrainment from both deep and mid-level cumulus

132 clouds dominated in the wave trough. Therefore, we hypothesize that shallow clouds near the EW
133 ridge are linked to an intensification of shallow circulation, and deeper clouds in the wave trough
134 are associated with a stronger deep circulation. This article is organized as follows: Section 2
135 presents the data and methods. Section 3 describes the synoptic variability and the horizontal and
136 vertical structure of EWs, followed by the moisture budget of the EWs in Section 4. The interac-
137 tion of EWs and the shallow and deep meridional circulations are presented in Section 5, and a
138 summary and conclusions are provided in Section 6.

139 **2. Data and methods**

140 *a. Data description*

141 We used hourly data from the ERA5 reanalysis (Hersbach and Dee 2016) with a horizontal grid
142 spacing of 0.25° and 37 pressure levels. The hourly ERA5 data were averaged to daily data. The
143 variables from ERA5 used in this study include horizontal and vertical winds, specific humidity,
144 temperature, and precipitation during the OTREC period (August 5 - October 3 of 2019).

145 Daily precipitation retrievals from the Global Precipitation Measurement (GPM) mission (Hou
146 et al. 2014) were also used. IMERG is a unified satellite precipitation dataset produced by NASA
147 to estimate surface precipitation over most of the globe (Huffman et al. 2015). Precipitation es-
148 timates from the GPM core satellite are used to calibrate precipitation estimates from microwave
149 and infrared sensors on other satellites. After merging the estimates from multiple satellites, sur-
150 face precipitation maps are produced at 0.1° horizontal resolution in the IMERG product.

151 We also used OTREC dropsondes from the NSF/NCAR Gulfstream V aircraft. Flight operations
152 for OTREC took place from 5 August to 3 October 2019. While other regions were also sampled,
153 twelve research flights (RFs) were performed over an East Pacific OTREC flight box (89° - 86° W,

154 3° - 11° N), a slightly smaller area than the OTREC region delineated in Fig. 1a. Each flight
155 lasted six hours, starting in the southern part of the box at 12 UTC and reaching the northern
156 part at 18 UTC. The flight pattern is shown in Figure 1 of Fuchs-Stone et al. (2020). Around
157 32 dropsondes were deployed during each flight from an altitude near 13 km. The dropsondes
158 collected measurements of horizontal winds, temperature, and humidity between the aircraft and
159 the surface with vertical resolution of around 0.5 hPa. We linearly interpolated the data to a
160 resolution of 20 hPa. As part of the OTREC field campaign, radiosondes in Santa Cruz, Costa
161 Rica (10.26° N, 85.58° W) were also launched between 20 August and 30 September 2019, at 00
162 and 12 UTC (6 am and 6 pm local time, respectively). OTREC dropsonde and sounding data were
163 sent to the Global Telecommunication System (GTS) and ERA5 reanalysis assimilated these data.

164 In addition to dropsondes, we utilized observations from the Hiaper cloud radar (HCR) installed
165 on the NSF/NCAR Gulfstream V aircraft (Rauber et al. 2017). HCR is a polarimetric, millimeter-
166 wavelength (W-band) radar that can detect light rain and ice and liquid clouds. It collects reflec-
167 tivity and Doppler radial velocity measurements, which at a vertical incident angle include the
168 vertical wind speed and particle fall speed. The aircraft flies at an average ground speed of 190
169 m s^{-1} , with a radar sampling rate of 0.1 s. All OTREC datasets were processed by the National
170 Center of Atmospheric Research (NCAR, Vömel et al. 2020).

171 Additionally, Geostationary Operational Environmental Satellite (GOES)-16 images were used
172 to complement OTREC dataset. GOES-16 is a current geostationary satellite operated by NOAA
173 and NASA and provides 16 spectral bands including 10 infrared (IR) channels. This study used
174 the GOES-16 longwave IR channel 14 with a 6 km resolution. GOES-16 images were processed
175 by NCAR/EOL and are available at <http://catalog.eol.ucar.edu/maps/otrec>.

176 *b. Identification of EWs*

177 The ERA5 and IMERG anomaly values used in the identification of the EWs were calculated
178 by removing the first three harmonics of the seasonal cycle based on the climatology between
179 1998 and 2018. Additionally, the OTREC period average was removed in order to **eliminate**
180 any decadal **or** interannual signal that may **have occurred** during this period. EWs during the
181 OTREC campaign were identified as follows. First, precipitation anomalies **and dynamical fields**
182 were filtered using a fast Fourier technique retaining wavenumbers between -20 to 0 and periods
183 between 2.5 and 10 days corresponding to EWs. This filtered domain **band** is also referred to as
184 tropical depression (TD) type disturbance region (Frank and Roundy 2006). Although this region
185 of wavenumber-frequency space includes both TD-type disturbances and mixed Rossby-gravity
186 (MRG) waves (Yokoyama and Takayabu 2012), we are confident that the features we **derived** are
187 EWs since the horizontal structure of winds and vorticity for each event **are also** consistent with
188 previous EW studies. Additionally, we used an extended time period **for this calculation** (from
189 June to November 2019) to minimize edge effects and **ensure no data loss due to filtering** for the
190 OTREC period.

191 We calculated the total precipitation and TD-band precipitation anomaly averaged over the
192 OTREC flight box (89° - 86° W, 3° - 11° N) and identified potential **convectively-active** EW events
193 when the total precipitation and TD-band precipitation anomaly were larger than the mean + 1.25
194 standard deviation. **While we begin our identification of EWs with strong filtered precipitation sig-**
195 **nals in the East Pacific ITCZ**, the potential EWs defined on the basis of precipitation were checked
196 to ensure they **were** also accompanied by strong **filtered** vorticity and meridional wind signals at
197 600 and 700 hPa that resemble EWs and not other westward propagating disturbances such as
198 MRG waves that have a similar phase speed but a different dynamical horizontal structure. In

199 particular, the **convectively-active** EWs selected had horizontal structures similar to those studied
200 by Serra et al. (2008) and Rydbeck and Maloney (2015). Additionally, we ensured that the wave
201 life cycle lasted more than two days as in Hodges (1995, 1999).

202 Figure 2 shows Hovmöller diagrams of **total and EW filtered anomalies for** precipitation, 600-
203 hPa vorticity, and 600-hPa meridional **wind in** the OTREC flight box. **The 700-hPa Hovmöller**
204 **diagrams look generally similar to the 600-hPa Hovmöller, and are not shown.** Based on the
205 criteria discussed above, we identified three **convectively-active** EWs in the Hovmöller precipita-
206 tion diagram accompanied by strong vorticity and meridional wind signals **that propagated from**
207 **southwest to northwest.** EWs 1 and 3 produced enhanced precipitation in the OTREC region on
208 7 August and 17 September, respectively, associated with positive vorticity anomalies at 600 hPa.
209 Southerly wind anomalies at 600 hPa **were** seen the next day. EW 2 produced enhanced precipita-
210 tion in the OTREC region on 15 August, and the strongest vorticity and southerly wind anomalies
211 **were** seen at 700 hPa (not shown). EWs 1 and 2 **showed** strong signals over the Caribbean at
212 day -1 and **seemed** to pass from the Caribbean to the East Pacific, although EW 3 **appeared** to
213 be generated in the East Pacific (not shown). Although vorticity and meridional winds **displayed**
214 westward propagation during the last two weeks of September, these propagating features **did not**
215 have a strong reflection in precipitation, **and hence are not analyzed further here.**

216 The total precipitation and TD-band precipitation anomaly time series over the OTREC flight
217 box are shown in Fig. 3. The **convectively-active** EWs identified had a strong positive precipitation
218 peak ($> 17 \text{ m d}^{-1}$), accompanied by cyclonic vorticity anomalies as seen in Fig. 2, followed
219 by suppressed precipitation two days later. There **were** two additional events that exceeded our
220 1.25 deviation standard threshold but, based on Fig. 2, **were not analyzed further** due to the lack
221 of vorticity and meridional wind signals (9 September) or unclear precipitation propagation (25
222 September). Two OTREC RFs coincided with the passage of the EWs we identified. The first

223 OTREC RF, on 7 August, corresponded to a day with enhanced precipitation associated with the
224 trough of the EW. The other OTREC RF, on 17 August, corresponded to a day with suppressed
225 precipitation associated with the ridge of the EW. Although OTREC RFs only partially captured
226 two EWs, ERA5 data was employed to study the three EWs previously identified with the IMERG
227 data. ERA5 assimilated all available dropsondes and intensive radiosonde operations occurred in
228 Costa Rica and Colombia during OTREC that provided further constraints on the reanalysis fields
229 for all EWs examined.

230 **3. Horizontal and vertical structure of the OTREC EWs**

231 *a. Composite EW structure*

232 Figures 4 and 5 show the composite precipitation during the passage of the three EWs. Precip-
233 itation at day 0 (Figs. 4a, 5c) corresponds to the precipitation averaged on 7 August, 15 August
234 and 17 September, when precipitation peaks in the OTREC region, and day +2 (Figs. 4b, 5h)
235 represents the suppressed precipitation phase two days later. On day 0, enhanced precipitation as-
236 sociated with the convective part of the EW was seen over the far East Pacific ITCZ centered over
237 the OTREC box. At day +2, the enhanced precipitation associated with the EW propagated north-
238 westward along the coast to 105°W, 17°N, while precipitation became suppressed in the OTREC
239 box. This northwestward propagation is confirmed in Fig. 5. The mean zonal phase speed of the
240 three EWs was estimated from the longitude-time diagram of composite precipitation for the lat-
241 itude range 3°-11°N, which corresponds to the OTREC flight box latitudes (Fig. 4c). Composite
242 precipitation associated with the EWs propagated westward at about 11.5 m s^{-1} between 80° and
243 115°W, although it was slower near 100°W. The zonal propagation of precipitation was seen both

244 in the total precipitation (Fig. 4c) and precipitation anomalies (Fig. 4d), although it should be
245 noted that there was also substantial meridional propagation (not shown).

246 Figure 5 shows the composite horizontal structure of EW precipitation anomalies and 600-hPa
247 horizontal wind anomalies and the north-south cross sections of vertical velocity and meridional
248 motion in the OTREC box from day -2 to day +3. We used vertical velocity as a proxy for
249 convective strength. Weak vertical velocities ($> -0.1 \text{ m s}^{-1}$) were seen at 90°W , 9°N especially
250 at low levels (below 600 hPa) due to the cold SSTs in this region (i.e., the Costa Rica dome, Xie
251 et al. 2005) that inhibit deep convection. At day -2 (Figs. 5a,d), positive precipitation anomalies of
252 about 10 mm d^{-1} were located in the ITCZ axis, with generally easterly 600-hPa wind anomalies.
253 Over the OTREC box, the vertical motion cross section suggests shallow and deep convection
254 similar to the August-September average cross section in Fig. 1b. Shallow convection associated
255 with a shallow meridional circulation was located at 850 hPa and 6°N , while deep convective
256 vertical motion associated with a deep meridional circulation was located at 300 hPa and 8°N .

257 At day -1 (Figs. 5b,e), enhanced precipitation (with anomalies larger than 30 mm d^{-1}) associated
258 with the EW trough (i.e., the center of maximum vorticity) was greatest at 80°W , slightly east of
259 the OTREC box. Over the OTREC box, ahead of the EW trough, the northerly flow at 850 hPa
260 associated with the shallow circulation weakened from 4 m s^{-1} at day -2 to 2 m s^{-1} at day -1
261 and the region of shallow vertical motion moved northward toward the region of deep convection.
262 The trough of the EW was associated with a transition of the shallow convection structure over
263 the OTREC box to a deep convective structure. Additionally, the anomalous wind field at 600 hPa
264 indicated a strengthening of the Caribbean low-level jet (CLLJ) during the passage of EWs with
265 easterly zonal wind anomalies around 5 m s^{-1} located near 15°N , 75°W that maximized at 925
266 hPa (not shown) and extended upward to 600 hPa (Martin and Schumacher 2011; Poveda et al.
267 2014; Rapp et al. 2014; Whitaker and Maloney 2018). The cyclonic circulation of EWs has been

268 associated with strengthening of the CLLJ easterly flow at 850 hPa (Molinari and Vollaro 2000),
269 which can then penetrate from the Caribbean into the Pacific through a gap in the mountains as
270 the Papagayo jet (Shapiro 1986; Molinari et al. 1997). The variations of the CLLJ during OTREC
271 are consistent with Whitaker and Maloney (2020) who showed the strengthening of the CLLJ
272 and Papagayo jet during the passage of an individual EW in the East Pacific. However, further
273 examination of the interactions between the CLLJ and EWs is outside the scope of this study.

274 At day 0 (Figs. 5c,f), the enhanced precipitation associated with the EW trough was located at
275 90°W, next to the OTREC box. The horizontal winds at 600 hPa were characterized by anomalous
276 cyclonic rotation and positive midlevel vorticity that supported deep convection and enhanced
277 precipitation. Raymond et al. (2014) used observational data over the tropics to show that mid-
278 level vortices modify the virtual temperature profile (i.e., cooler below the mid-level vortex and
279 warmer above) to create low-level instability that fosters strong low-level convergence and subse-
280 quent deep convection. Over the OTREC box, the deep circulation was dominant compared to the
281 shallow circulation. The vertical velocity peak was centered at 400 hPa and 8°N, indicating a strat-
282 iform profile (Schumacher et al. 2004). A weak shallow vertical velocity peak also existed at day
283 0, consistent with the presence of updrafts in convective elements that accompany the stratiform
284 features, as noted in previous studies (Masunaga and Luo 2016).

285 At day +1 (Figs. 5g,j), enhanced precipitation associated with the trough of the EW moved to
286 100°W, a few degrees west of the OTREC box, and the circulation field was oriented southwest -
287 northeast. Over the OTREC box and behind the EW trough center, the vertical motion associated
288 with deep convection was still strong but weaker compared to the previous day, and the shallow
289 circulation was still muted. The deep convection was likely maintained by the enhanced mid-
290 level southerly inflow associated with the cyclonic circulation of the EW that brings horizontal
291 convergence (Huaman and Takahashi 2016; Nolan et al. 2007, 2010). At day +2 (Figs. 5h,k),

292 the enhanced precipitation associated with the EW trough was centered at 110°W, 15°N, and
293 suppressed precipitation and associated negative vorticity anomalies in the EW ridge (i.e., the
294 center of minimum vorticity) were predominant over the OTREC box. The EW circulation was
295 oriented west-east at day 0, but developed a southwest-northeast tilt on subsequent days. This tilted
296 structure has been argued by previous studies to be associated with vortex stretching and horizontal
297 elongation from southwest to northeast of the dynamical signature of the wave (Rydbeck and
298 Maloney 2015). The cross section over the OTREC box shows suppressed deep convection and a
299 pronounced shallow circulation with a strong overturning circulation at 850 hPa (i.e., meridional
300 winds larger than 7 m s^{-1}) south of 6°N. This shallow circulation became deeper and strengthened
301 at day +3 (Figs. 5i,l). The composite analysis suggests strong modification of the shallow and
302 deep circulations during the passage of EWs, including intensification of the deep circulation at
303 day +0 and shallow circulation at days +2 and +3. All three EWs examined during OTREC have
304 qualitatively similar modulation of the deep and shallow circulations (Figs. S1, S2, and S3). The
305 mechanisms through which the deep and shallow circulations are modulated by the passage of the
306 EWs will be discussed in section 5.

307 The vertical structure of EWs at the two latitude ranges where the deep and shallow circulations
308 predominated will now be described. Figure 6 shows time-height diagrams of anomalous ERA5
309 vorticity, specific humidity, meridional wind, and vertical velocity composited for the three EWs
310 over the northern part of the OTREC box (7 - 11°N) where the deep circulation in the ITCZ was
311 dominant (Figs. 6a-d) and the southern part of the OTREC box (3 - 7°N) where the shallow
312 circulation was dominant (Figs. 6e-h). We note that the composite evolution of the EW vertical
313 structure during the OTREC campaign in the northern part of the ITCZ is consistent with Serra
314 et al. (2008).

315 At days - 2 and -1, ahead of the EW trough, positive vorticity (Fig. 6a), positive humidity anomalies (Fig. 6b), and northerly winds (Fig. 6c) occurred below 600 hPa between 7 - 10°N, with upward vertical motion anomalies throughout the troposphere (Fig. 6d). However, the southern part 317 of the OTREC box (3 - 7°N) was not as strongly impacted by the EWs, and the vorticity (Fig. 6e), 318 meridional wind (Fig. 6g), and upward motion (Fig. 6h) anomalies were weak. At day 0, within 319 the convective part of the EW, positive vorticity and strong upward vertical velocity anomalies 320 occurred throughout the troposphere between 7 - 10°N, with positive specific humidity anomalies 321 lies above 800 hPa and negative specific humidity anomalies below 800 hPa. The meridional 322 wind anomalies suggest a strengthening of the deep meridional circulation, with intensification of 323 the upper-level (200 hPa) meridional outflow and low to mid-level meridional inflow, especially 324 around 600 hPa where anomalies were up to 5 m s^{-1} . This structure is consistent with convective 325 and stratiform structures in MCSs with deep circulations (Whitaker and Maloney 2020) and in 326 other equatorial disturbances (Kiladis et al. 2009). However, in the southern part of the OTREC 327 box, the vorticity and upward vertical motion anomalies were weak throughout the troposphere 328 at day 0, which suggests only weak impact of EWs on shallow convection and associated circu- 329 lations at these latitudes. At day +2, behind the trough of the EW, negative vorticity anomalies 330 and downward anomalous vertical motion were seen throughout the troposphere with anomalous 331 northerly winds at mid-levels between 7 - 10°N. In the southern part, positive vorticity anomalies 332 and positive specific humidity anomalies occurred, with strong meridional outflow around 800 hPa 333 characterized by anomalies up to 4 m s^{-1} and shallow upward vertical motion that intensified until 334 day +3, suggesting significant impacts on shallow convection and associated circulations at these 335 latitudes. The vertical structure of the EWs between 7 - 10°N from ERA5 was consistent with the 336 vertical structure of EW 3 derived using OTREC radiosondes from Santa Cruz, Costa Rica (not 337 shown).

339 *b. Individual EWs*

340 We now analyze the individual EW events using the OTREC field campaign observations, sup-
341 plemented by ERA5 and GOES IR imagery. Two RFs occurred during the passage of EWs (Figs.
342 2 and 3). During OTREC RF 1 (7 August), the NSF/NCAR Gulfstream V aircraft flew in the
343 region of enhanced precipitation associated with **the trough** of EW 1. During OTREC RF 5 (17
344 August), the aircraft flew in the suppressed precipitation **associated with the ridge** of EW 2.

345 Figure 7 shows **the air temperature** (red) and dewpoint **temperature** (blue) profiles at days 0 and
346 +2 at 8°N and 4°N during all three EWs from ERA5 and OTREC. We used OTREC dropsondes
347 from two RFs and **used** profiles from ERA5 **for the other times. ERA5 profiles are similar to the**
348 **OTREC profiles during the August 7 and August 17 events shown here (Fig. S4).** Table 1 shows
349 the lifting condensation level (LCL), convective available potential energy (CAPE), and convective
350 inhibition (CIN) values for each day and latitude.

351 At day 0 and 8°N (Fig. 7a), the soundings **showed** moist conditions throughout the troposphere
352 associated with the convectively active part of the EWs (Figs. 5c,f). Table 1 indicates that the LCL
353 **was** around 970 hPa in each EW, CAPE **was** 1934 J kg^{-1} for EW 1 and around 1185 J kg^{-1} for
354 the other two EWs, while CIN **was** 0 J kg^{-1} **for all** EWs. At day +2 (Fig. 7b), when the **composite**
355 **EW trough** **had** moved west and there **was** no longer a deep meridional circulation (Figs. 5h,k), a
356 shallow moist layer **was** seen between 1000 and 900 hPa, with drier conditions above, especially
357 during EW 1. The LCL **varied** between 956 hPa and 975 hPa, making the LCL slightly higher in
358 two of the three EWs (i.e., EW 1 and EW 3) **at day +2** compared to day 0. CAPE **increased** in EW
359 2 and EW 3 at day 2, reaching 2260 J kg^{-1} in EW 2. **This large value indicates that this index is**
360 **inadequate by itself for detecting the potential for deep convection, as found in other studies (e.g.,**

361 Sherwood et al. 2004), since suppressed convection is associated with the ridge of the EW (Fig,
362 5h). CIN remained zero in all three EWs at day +2.

363 At day 0 and 4°N (Fig. 7c), which represented conditions south of the main precipitation area of
364 the convectively-active EW, there was a layer of moist air below 800 hPa, consistent with shallow
365 convection driven by the strong meridional SST gradients (Back and Bretherton 2009). Dry air
366 predominated aloft, especially between 500 and 300 hPa. The temperature profiles also suggested
367 a weak trade wind inversion between 950 and 850 hPa. Table 1 shows that the LCLs were similar
368 to 8°N values but that CAPE was substantially less, with values ranging from 62 to 395 J kg⁻¹,
369 and CIN was strongly negative with values ranging from -36 to -68 J kg⁻¹. At day +2 (Fig.
370 7d), the low-level moist layer extended up to 800 hPa and was capped by a stronger trade wind
371 inversion between 850 and 750 hPa, which was higher than on day 0. Conditions remained dry
372 aloft. LCL heights became higher in EW 1 and EW 3 and CAPE increased in EW 2 and EW 3
373 (similar to the day 0 to day +2 trends at 8°N). CIN was less strongly negative compared to day 0
374 except in EW 3.

375 Figure 7 and Table 1 indicate that the thermodynamic structure variations of the three EWs
376 between days 0 and +2 was qualitatively similar, although the magnitude of the variations showed
377 substantial differences across events. Of note is a larger spread in the dew point profiles at the mid
378 and upper levels than in the temperature profiles, and this difference became more pronounced at
379 4°N. While it could be argued that some of this variability was introduced by only assimilating
380 OTREC dropsondes in a subset of the profiles, the very strong dry air layer during EW 1 exists
381 in the ERA5 profiles two days after the OTREC dropsondes were assimilated so it appears that
382 the ERA5 reanalysis can successfully represent EW structure and its variability to some extent.
383 The OTREC dropsondes launched through cloudy vs clear air may also account for some of this
384 difference.

385 We now examine the convective structures seen by the HCR, the cloud radar installed on the
386 NSF/NCAR Gulfstream V aircraft. On 7 August, RF 1 sampled a large MCS located in the north-
387 ern part of the OTREC box (Fig. 8a). In regions of deep convective structures and stratiform
388 rain regions with a well-defined bright band near an altitude of 4.5 km (Fig. 8c), the radar was
389 strongly attenuated in the lower troposphere given the nature of W-band retrievals in deep convec-
390 tive systems. The southern part of the OTREC box did not show deep convection (Fig. 8b) and
391 was impacted by very dry mid-level air (Fig. 7c). The HCR observed shallow cumulus clouds with
392 echo-top heights around 1 km (or 900 hPa) and cirrus clouds near 10 km (Fig. 8d). On 17 August,
393 RF 3 sampled suppressed convection in the northern part of the OTREC box associated with the
394 non convective part of the EW that passed through two days before (Fig. 8e). The HCR detected
395 isolated convective cells with echo-top heights near 6 km (Fig. 8g). In the southern part of the
396 OTREC box (Fig. 8f), the HCR observed shallow cumulus clouds with echo-top heights at 1.5 km
397 (or 850 hPa) and cirrus clouds at 10 km. The shallow cumulus extended slightly higher than those
398 seen during RF1, potentially because of the elevated trade inversion at day +2 (cf. Figs. 7c and d).
399 Therefore, deep convection in the northern part of the OTREC box and muted shallow convection
400 in the southern part of the OTREC box dominated at day 0 when the trough center of the EW
401 was near. Deep convection at day 0 was accompanied by an enhanced deep circulation (Fig. 5f).
402 Suppressed deep convection in the northern part of the OTREC box and enhanced shallow con-
403 vection in the southern part of the OTREC box dominated at day +2 with the EW ridge passage.
404 The shallow convection at day +2 was accompanied by a strong shallow circulation (Fig. 5k). We
405 performed a separate analysis with radar observations from the GPM satellite over the East Pacific
406 OTREC box during the three EWs and also found stronger and deeper shallow structures in the
407 southern part of the ITCZ at day +2 compared to day 0 (not shown).

408 **4. Moisture budget**

409 In this section, the moisture budget is examined to help understand why convection varies as
410 a function of EW phase in climatologically shallow and deep regions. Many previous studies
411 have shown that convection is favored when the lower free troposphere is moist (e.g., Raymond
412 et al. 1998; Holloway and Neelin 2009). Rydbeck and Maloney (2015) further suggest that the
413 distribution of convection within EWs is strongly constrained by the moisture field. The moisture
414 budget is represented as:

$$\left[\frac{\delta q}{\delta t} \right] = -[v_h \cdot \nabla_h q] - \left[\omega \frac{\delta q}{\delta p} \right] + E - P \quad (1)$$

415 where q is specific humidity, v_h is horizontal wind, ω is vertical velocity, E is evaporation
416 and P is precipitation. The brackets represent the mass-weighted vertical integral from 1000 to
417 200 hPa. The term on the left-hand side of Eq. (1) represents the vertically integrated specific
418 humidity tendency. The first term on the right-hand side of Eq. (1) is the moisture tendency
419 resulting from horizontal advection. The second term on the right-hand side is the moistening
420 by vertical advection. The third and fourth terms on the right-hand side are the column moisture
421 tendency as a result of surface evaporation and precipitation, respectively. In this study, we do
422 not explicitly examine E because it was previously shown to be of second order importance for
423 determining the EW modulation of convection (Rydbeck and Maloney 2015). Vertical advection
424 minus precipitation has parallels to the sum of vertical advection and radiation in the column-
425 integrated MSE budget, and has been referred to as the “column process” by some studies (e.g.,
426 Wolding et al. 2016).

427 The vertically integrated moisture budget has been used to study regions with large precipi-
428 tation produced by EWs. For example, Rydbeck and Maloney (2015) showed that anomalous

429 horizontal advection has large contributions to the positive tendency of column-integrated mois-
430 ture tendencies ahead of the EW convection, and to negative moisture tendencies behind the EW
431 convection. Ahead of the cyclonic EW center, northeasterly flow advects moist air from the East
432 Pacific warm pool, and behind the cyclonic EW center, southwesterly flow advects dry air from
433 the East Pacific cold tongue. They also examined the difference between the tendency resulting
434 from vertical advection and precipitation, formulated as the residual of the other terms in the bud-
435 get and sometimes related to the “column process” in the atmospheric science literature. Positive
436 regions of this quantity indicate where anomalous vertical advection is moistening the atmosphere
437 more than anomalous drying by precipitation. Rydbeck and Maloney (2015) showed that while
438 moistening not counteracted by precipitation preferentially occurs ahead of the wave trough, verti-
439 cal advection minus precipitation is anomalously negative behind the wave trough. The difference
440 between vertical advection and precipitation is substantially smaller than the total moisture ten-
441 dency, suggesting that horizontal advection is the largest contributor to the positive tendency of
442 column-integrated moisture tendencies ahead of EW convection.

443 This previous work implies in the context of the current study that shallow, non-precipitating
444 convection might play a moistening role ahead of the wave because of anomalously large low-level
445 moisture convergence and suppressed precipitation. On the other hand, regions of stratiform rain
446 from deep convection with muted low-level moisture convergence and large precipitation might
447 play a drying role behind the wave. Figure 9 shows the composite moisture tendency anom-
448 alies resulting from horizontal advection and from vertical advection minus precipitation. We used
449 precipitation from ERA5 in the moisture budget rather than IMERG because of the better phys-
450 ical consistency with the convergence field. The spatial structure of the ERA5 precipitation was
451 generally consistent with IMERG precipitation structure (Fig. 5). However, ERA5 precipitation

452 anomalies are weaker and are up to 20% lower than the IMERG precipitation anomalies within
453 the EW at days -1, 0, and +1 (not shown).

454 At day -1 (Fig. 9a), the enhanced precipitation associated with the EW **trough was** located
455 at 80°W and ERA5 precipitation (blue contours) showed a zonal band of precipitation at 8°N.
456 While dynamical features resembling an EW at day -1 are generally weak, positive horizontal
457 advection anomalies (shaded) **were** slightly less than 3 mm d⁻¹ ahead of the wave (i.e., **west of**
458 **the trough axis**) and around -5 mm d⁻¹ behind the wave (i.e., **east of the trough axis**) near the
459 South American coast. The difference between the vertical advection and precipitation (Fig. 9f)
460 indicates anomalous moistening to the northwest (83°W, 10°N) of the convectively-active part of
461 the EW trough. At day 0 (Fig. 5c), enhanced precipitation was associated with the EW trough
462 centered near 90°W, next to the OTREC box. Negative horizontal advection anomalies increased
463 over the southeastern part of this convectively active region (Fig. 9b). The vertical advection
464 and precipitation mostly cancel each other at the EW trough axis (around 90°W, Fig. 9g), but
465 moistening by vertical advection exceeded drying by precipitation ahead of the wave, suggesting a
466 region with large low-level convergence and weak precipitation (i.e., cumulus congestus). Behind
467 the wave, anomalous precipitation exceeded vertical advection, resulting in drying, suggesting
468 a region with anomalously weak low-level convergence and enhanced precipitation (stratiform
469 structures). These horizontal patterns, **while noisier given the smaller sample size**, are consistent
470 with Rydbeck and Maloney (2015) and propagated westward in association with the EW.

471 At day +1 (Fig. 9c), enhanced circulation and precipitation associated with the EW trough were
472 oriented southwest-northeast. **The EW trough was** centered at 100°W, **with** anomalous **negative**
473 **horizontal moisture** advection behind the wave **trough** also oriented **southwest-northeast**. Over the
474 OTREC box, anomalously **negative** horizontal **moisture** advection and 600-hPa southerly winds
475 **were** predominant, consistent with intrusion of dry air from the equatorial region of the SST cold

476 tongue. The difference between anomalous vertical advection and precipitation (Fig. 9h) suggests
477 moistening by vertical advection exceeded drying by precipitation ahead of the wave. Behind the
478 wave **trough**, precipitation exceeded vertical advection, resulting in drying. This behavior suggests
479 shallow and stratiform structures ahead **of** and behind the wave **trough**, respectively. The stratiform
480 structure behind the wave **trough** is consistent with Fig. 5j.

481 At days +2 and +3 (Figs. 9d and e), the convectively active part of the southwest-northeast
482 oriented EW **was** centered around 110°W and 115°W (**i.e.**, **the trough**), respectively. As on the
483 previous days, anomalous **negative** horizontal **moisture** advection **was** observed behind the wave.
484 Over the OTREC box, the precipitation **was** suppressed. In the northern part of the OTREC box,
485 **anomalous negative** horizontal **moisture** advection predominated**d**, and in the southern part, **anoma-**
486 **lous positive** horizontal **moisture** advection predominated**d**. Since the EW **was** tilted with height,
487 **the time-height diagram in Fig. 6g can also be interpreted as longitude-height diagram**. The hor-
488 **izontal flow was** mainly northerly at 850 hPa **in the southern part** and **this was** the main source
489 of moistening. The structure of the horizontal advection field likely played**d** an important role in
490 regulating local shallow convection and circulation near $4\text{-}5^{\circ}\text{N}$ (Figs. 5h-l, 8h). The difference
491 between the vertical advection and precipitation (Figs. 9i and j) shows **that** moistening by vertical
492 advection **was** small over the OTREC box at day +2 and positive around 5°N at day +3, **also sug-**
493 **gesting the importance of shallow convection there (Fig. 8h)** for fostering column moistening **in**
494 **addition to horizontal advection**.

495 Figures 10a and b show the EW composite time-latitude plots of omega at 400 and 900 hPa
496 that display deep and shallow convective structure evolution, respectively. In the OTREC average
497 (Fig. 1), omega peaks at 400 and 900 hPa **were** located at 8.5° and 5°N , respectively (dashed
498 lines in Figs. 10a and b). The vertical and horizontal advection of MSE calculated as in Back
499 and Bretherton (2006) are shown in Figs. 10c and d. **MSE is a thermodynamic variable that helps**

500 explain the interactions between convection and the large-scale circulation. The MSE budget has
501 an advantage over the moisture budget in the deep tropics where temperature gradients are weak
502 in that it accounts for the cancellation of vertical moisture advection and drying by precipitation in
503 the its vertical advection term, especially when considered in conjunction with radiation (Wolding
504 and Maloney 2015). Additionally, the vertical advection of MSE is strongly related to the shape of
505 the vertical motion profile in the ITCZ, and its use provides direct comparison to studies involving
506 the vertical structure of the ITCZ and moist static stability (Back and Bretherton 2006; Inoue
507 and Back 2015). Positive values indicate an import of MSE and maximum vertical velocity at
508 low levels (i.e., a bottom-heavy structure), and negative values indicate the export of MSE with
509 maximum vertical velocity at high levels (i.e., a top-heavy structure). Additionally, the moisture
510 tendency resulting from vertical and horizontal advection (section 4) are shown in Figs. 10e and f,
511 respectively. Vertical advection minus precipitation is shown in contours in Figure 10e.

512 For the deep convection regime at day 0 (Fig. 10a), the upper-level vertical velocity at 8°N is
513 enhanced, associated with an anomalous export of MSE through vertical advection (Fig. 10c). The
514 export of MSE suggests that precipitation was stronger than vertical moisture advection, consistent
515 with Fig. 10e (contours). For the climatological shallow convection region near 4-5°N, where the
516 upward vertical motion is generally stronger at 900 hPa compared to 400 hPa, shallow convection
517 was inhibited at day 0, especially at 4°N (Fig. 10b), with enhanced shallow convection at days +2
518 and +3 (cf. Figs. 5k-l). At day +2, the shallow convection region was associated with anomalous
519 import of MSE ($+100 \text{ W m}^{-2}$) and a positive moisture tendency resulting from horizontal advection
520 (Figs. 10d and f) consistent with a deepening of the shallow clouds as suggested by the HCR data
521 (Fig. 8h). The horizontal advection of MSE and the moisture tendency resulting from horizontal
522 advection changed from negative values ($< -150 \text{ W m}^{-2}$ and -4 mm d^{-1}) at day 0 to positive
523 values ($+100 \text{ W m}^{-1}$ and $+3 \text{ mm d}^{-1}$) at days +2 and +3. It is interesting to note that although

524 the strongest shallow meridional overturning occurred on day +2 (Fig. 5k), the largest low-level
525 vertical velocity occurred at day +3 (Fig. 5l). At day +3, the vertical moisture advection term was
526 larger than the precipitation (Fig. 10e), consistent with the positive anomalous MSE import and
527 indicative of the stronger congestus structures with large lower tropospheric vertical velocity.

528 5. EWs and the shallow and deep meridional circulations

529 The horizontal and vertical structure of EWs and associated moisture tendency fields suggest
530 substantial perturbations to the climatological deep and shallow circulations during wave passage
531 (Figs. 5, 8 and 9). In this section, we discuss mechanisms responsible for the modification of deep
532 and shallow circulations during the passage of EW. Figures 11a-d show total vertical velocity and
533 relative humidity cross sections during the enhanced (day 0) and suppressed (day +2) convection
534 periods associated with the passage of EWs across the OTREC box.

535 At day 0, a deep circulation was observed in the ITCZ around 8°N with surface southerly inflow
536 and return upper-level northerly outflow (Fig. 11a) and high relative humidity throughout the
537 troposphere (Fig. 11c). The moisture tendency anomaly resulting from vertical advection was
538 positive (8 mm d^{-1}) in this deep convection region (Fig. 11e). Dry inflow between 600 and
539 400 hPa (Figs. 7c and 11c) was also observed that could have induced a positive feedback to
540 a deep convective structure by inducing temperature anomalies as proposed by Zuidema et al.
541 (2006) and Nolan and Rappin (2008). However, in the southern part of the ITCZ, where a shallow
542 circulation is found in the climatology (i.e., around 6°N), negative horizontal moisture and MSE
543 advection anomalies were apparent and likely inhibited shallow convection (Fig. 8d). The shallow
544 circulation had a weak northerly overturning flow at 850 hPa between 3 and 6°N associated with
545 the cyclonic circulation around the trough of the EW that provided southerly wind anomalies (Fig.
546 11e) and weakened the shallow circulation overturning flow (Fig. 11a).

547 At day +2, the deep circulation **was** muted but a strong shallow circulation south of 5°N **was**
548 observed with strong overturning northerly flow at 850 hPa (Fig. 11b). The shallow circulation
549 associated with the shallow convection **was likely inhibited from** transitioning to deep convection
550 due to the dry mid and upper level conditions imposed by the non convectively **active** part of the
551 EW (Fig. 11d). The climatological ITCZ axis (8 °N) **was** dominated by a negative tendency due
552 to vertical advection and deep convection **was** also suppressed (Fig. 11f). However, horizontal
553 advection anomalies **were** positive south of 5°N and **likely helped** maintain the shallow convection
554 at day +2 (Fig. 8h). The strong northerly shallow overturning flow at 850 hPa **was** part of the EW
555 horizontal structure **that showed** an anticyclonic circulation with strong northerly flow at day +2
556 (Fig. 11f). The anticyclonic circulation **was** vertically tilted, **with** northerly flow at 850 hPa (600
557 hPa) **that reached** the OTREC box at day +2 (+3) as shown in Fig. 6. Additionally, the difference
558 between vertical advection and precipitation suggests that this region was dominated by shallow
559 structures **that produced** weak precipitation (i.e., shallow cumulus and stratocumulus clouds) **but**
560 **relatively strong low-level convergence** at days +2 and +3 (Figs. 8h and 9i,j).

561 To show the consistency of the three EWs in modifying the climatological deep and shallow
562 circulations in the East Pacific ITCZ, Fig. 12 compares the meridional wind profile of each wave
563 at days 0 and +2 at 4 - 5°N (the shallow circulation region) and 7 - 8 °N (the deep circulation
564 region) with the August-September 2019 mean profile. On day 0 at 7 - 8°N (Fig. 12a), a deep
565 circulation with southerly winds at low levels and northerly winds at upper levels **was** consistently
566 **produced** across the three EWs. The deep circulations during the passage of EWs **were** stronger
567 compared to the August-September average, especially during EW 1 and 2 **with stronger low-level**
568 **inflow**. On day 0 at 4 - 5°N (Fig. 12c), there **was** weaker overturning flow **near** 800 hPa in the
569 EWs compared to the August-September profile. At day +2, the deep circulation **was** weaker at 7 -

570 8°N (Fig. 12b), but the overturning flow around 800 hPa **at 4 - 5°N was** stronger after the passage
571 **of the EWs** compared to the August-September profile (Fig. 12d).

572 **6. Summary and conclusions**

573 This study aimed to identify **synoptic variability associated with** EWs during the OTREC field
574 campaign, and determine their impacts on the climatological deep and shallow circulations in the
575 East Pacific. Using OTREC observations, ERA5 reanalysis, and satellite precipitation **estimates**,
576 we identified three strong EWs with consistent **mid-level** vorticity and meridional wind structures.
577 Modulation of the climatological shallow and deep circulations in the far East Pacific **at longitudes**
578 **near the OTREC box** were found during the passage of EWs, which we depict as a schematic in
579 Fig. 13. Normal conditions (Fig. 13a) represent the August-September 2019 mean (Fig. 1b),
580 with a shallow circulation **near** 6°N below 850 hPa and a deep circulation at 8°N between the
581 surface and 200 hPa. Positive low-level vorticity (i.e., cyclonic circulation) **is also characteristic of**
582 **climatological conditions** (Raymond et al. 2014), **with** associated surface westerly winds at 7°N.
583 Easterly winds **occur** near the equator between 700 and 600 hPa.

584 The EWs during OTREC strongly modulated these seasonal mean conditions. At day -1 of the
585 EW evolution (Fig. 13b), deep convection was enhanced at 8°N and the total low-level positive
586 vorticity (Fig. 6a) was stronger than climatology and associated with intensified near-surface west-
587 erly flow. At day 0 (Fig. 13c), the trough of the EW was associated with enhanced deep convection
588 and a deep circulation at 8°N and shallow convection was displaced north of 6°N. Positive vor-
589 ticity predominated near the surface and at 600 hPa in the region of deep convection, associated
590 with intensifying near-surface westerly flow just to the south of the deep convective region. At
591 day +1 after the passage of the trough (Fig. 13d), deep convection decayed and stratiform clouds
592 predominated at 8°N, with the net effect of vertical moisture advection and precipitation produc-

593 ing drying. Enhanced mid-level southerly inflow associated with the EW structure (Figs. 5g,j) and
594 upper level northerly outflow also occurred. At day +2 (Fig. 13e), the ridge of the EW was associ-
595 ated with suppressed deep convection and downward motion at 8°N in the anticyclonic circulation
596 region of the EW, and the same anticyclonic circulation enhanced the mid-level easterly flow near
597 the equator. The positive low-level vorticity became weaker and a strong shallow circulation with
598 increased shallow convection was observed at 4°N. The strong shallow overturning circulation at
599 850 hPa was associated with an EW structure that drove strong northerly winds between 700 and
600 800 hPa (Fig. 6b). At day +3 (Fig. 13f), weak convection was observed at 8°N, although the
601 positive low-level vorticity recovered. The shallow circulation was still prominent associated with
602 deeper and stronger shallow convection.

603 This schematic is consistent with the climatological deep and shallow circulations being mod-
604 ified by the passage of EWs in the East Pacific. The trough of the EW enhanced the ITCZ deep
605 circulation at day 0 and was associated with an export of column integrated MSE by vertical ad-
606 vection; however, the shallow circulation in the southern part of the ITCZ was weak due to a
607 negative moisture tendency from horizontal advection over the southern part of the ITCZ. On the
608 other hand, the suppressed part of the EW enhanced the shallow circulation at day +2. The shal-
609 low overturning flow at 850 hPa was linked to the anticyclonic circulation of the EW. A positive
610 anomalous moisture tendency that resulted from horizontal advection and import of MSE helped
611 drive shallow convection over the southern part of the ITCZ. This MSE import was consistent with
612 moistening by vertical advection that outpaced precipitation, which suggestive of an enhancement
613 of shallow convection that fostered column moistening at day +3. Our results indicate that the
614 three EWs altered the East Pacific ITCZ circulation in a consistent way. Even though ERA5 did
615 not assimilate OTREC data during all the EWs, it appears capable of capturing the salient struc-
616 tures and variations of the EWs during this time. Future work will involve the identification of

617 EWs during a longer time period using satellite precipitation and ERA5 to confirm the systematic
618 alteration of the shallow and deep circulation during the passage of EWs in the East Pacific ITCZ.

619 *Acknowledgments.* The authors thank Z. Fuchs, D. Raymond and the rest of the OTREC team for
620 interesting discussions that improved this study. **We also thank the reviewers for their constructive**
621 **comments that helped to improve this manuscript.** This work has been supported by NASA Earth
622 and Space Science Fellowship (NESSF) under grant 80NSSC18K1402P00001. EDM was sup-
623 ported by NSF Climate and Large-Scale Dynamics grant AGS-1735978 **and by NASA CYGNSS**
624 **grant NNX17AH77G.**

625 References

- 626 Back, L., and C. Bretherton, 2006: Geographic variability in the export of moist static energy and
627 vertical motion profiles in the tropical Pacific. *Geophysical Research Letters*, **33** (17).
- 628 Back, L. E., and C. S. Bretherton, 2009: On the relationship between SST gradients, boundary
629 layer winds, and convergence over the tropical oceans. *Journal of Climate*, **22** (15), 4182–4196.
- 630 Berry, G., C. Thorncroft, and T. Hewson, 2007: African easterly waves during 2004—Analysis
631 using objective techniques. *Monthly Weather Review*, **135** (4), 1251–1267.
- 632 Dominguez, C., J. M. Done, and C. L. Bruyère, 2020: Easterly wave contributions to seasonal
633 rainfall over the tropical Americas in observations and a regional climate model. *Climate Dy-
634 namics*, **54** (1-2), 191–209.
- 635 Frank, W. M., and P. E. Roundy, 2006: The role of tropical waves in tropical cyclogenesis. *Monthly
636 Weather Review*, **134** (9), 2397–2417.
- 637 Fuchs-Stone, Ž., D. J. Raymond, and S. Sentić, 2020: OTREC2019: Convection over the East
638 Pacific and Southwest Caribbean. *Geophysical Research Letters*, **47** (11), e2020GL087 564.

- 639 Gomes, H. B., T. Ambrizzi, B. F. P. da Silva, K. Hodges, P. L. S. Dias, D. L. Herdies, M. C. L.
640 Silva, and H. B. Gomes, 2019: Climatology of easterly wave disturbances over the tropical
641 South Atlantic. *Climate Dynamics*, **53 (3-4)**, 1393–1411.
- 642 Handlos, Z. J., and L. E. Back, 2014: Estimating vertical motion profile shape within tropical
643 weather states over the oceans. *Journal of Climate*, **27 (20)**, 7667–7686.
- 644 Hersbach, H., and D. Dee, 2016: ERA5 reanalysis is in production. *ECMWF newsletter*, **147 (7)**,
645 5–6.
- 646 Hodges, K., 1995: Feature tracking on the unit sphere. *Monthly Weather Review*, **123 (12)**, 3458–
647 3465.
- 648 Hodges, K., 1999: Adaptive constraints for feature tracking. *Monthly Weather Review*, **127 (6)**,
649 1362–1373.
- 650 Holloway, C. E., and J. D. Neelin, 2009: Moisture vertical structure, column water vapor, and
651 tropical deep convection. *Journal of the atmospheric sciences*, **66 (6)**, 1665–1683.
- 652 Hou, A. Y., and Coauthors, 2014: The global precipitation measurement mission. *Bulletin of the
653 American Meteorological Society*, **95 (5)**, 701–722.
- 654 Huaman, L., and C. Schumacher, 2018: Assessing the vertical latent heating structure of the East
655 Pacific ITCZ using the CloudSat CPR and TRMM PR. *Journal of Climate*, **31 (7)**, 2563–2577.
- 656 Huaman, L., C. Schumacher, and G. N. Kiladis, 2020: Eastward propagating disturbances in the
657 tropical Pacific. *Monthly Weather Review*.
- 658 Huaman, L., and K. Takahashi, 2016: The vertical structure of the eastern Pacific ITCZs and asso-
659 ciated circulation using the TRMM Precipitation Radar and in situ data. *Geophysical Research
660 Letters*, **43 (15)**, 8230–8239.

- 661 Huffman, G. J., D. T. Bolvin, D. Braithwaite, K. Hsu, R. Joyce, P. Xie, and S.-H. Yoo, 2015:
662 NASA global precipitation measurement (GPM) integrated multi-satellite retrievals for GPM
663 (IMERG). *Algorithm Theoretical Basis Document (ATBD) Version, 4*, 26.
- 664 Inoue, K., and L. Back, 2015: Column-integrated moist static energy budget analysis on various
665 time scales during TOGA COARE. *Journal of the Atmospheric Sciences*, **72** (5), 1856–1871.
- 666 Janiga, M. A., and C. D. Thorncroft, 2013: Regional differences in the kinematic and thermo-
667 dynamic structure of African easterly waves. *Quarterly Journal of the Royal Meteorological
668 Society*, **139** (675), 1598–1614.
- 669 Jaramillo, L., G. Poveda, and J. F. Mejía, 2017: Mesoscale convective systems and other precipita-
670 tion features over the tropical Americas and surrounding seas as seen by TRMM. *International
671 Journal of Climatology*, **37**, 380–397.
- 672 Kiladis, G. N., C. D. Thorncroft, and N. M. Hall, 2006: Three-dimensional structure and dynamics
673 of African easterly waves. Part I: Observations. *Journal of the Atmospheric Sciences*, **63** (9),
674 2212–2230.
- 675 Kiladis, G. N., M. C. Wheeler, P. T. Haertel, K. H. Straub, and P. E. Roundy, 2009: Convectively
676 coupled equatorial waves. *Reviews of Geophysics*, **47** (2).
- 677 Lindzen, R. S., and S. Nigam, 1987: On the role of sea surface temperature gradients in forcing
678 low-level winds and convergence in the tropics. *Journal of the Atmospheric Sciences*, **44** (17),
679 2418–2436.
- 680 Martin, E. R., and C. Schumacher, 2011: Modulation of Caribbean precipitation by the Madden-
681 Julian oscillation. *Journal of Climate*, **24** (3), 813–824.

- 682 Masunaga, H., and Z. J. Luo, 2016: Convective and large-scale mass flux profiles over tropical
683 oceans determined from synergistic analysis of a suite of satellite observations. *Journal of Geo-*
684 *physical Research: Atmospheres*, **121** (13), 7958–7974.
- 685 Molinari, J., D. Knight, M. Dickinson, D. Vollaro, and S. Skubis, 1997: Potential vorticity, easterly
686 waves, and eastern Pacific tropical cyclogenesis. *Monthly Weather Review*, **125** (10), 2699–
687 2708.
- 688 Molinari, J., and D. Vollaro, 2000: Planetary-and synoptic-scale influences on eastern Pacific
689 tropical cyclogenesis. *Monthly Weather Review*, **128** (9), 3296–3307.
- 690 Nolan, D. S., S. W. Powell, C. Zhang, and B. E. Mapes, 2010: Idealized simulations of the
691 intertropical convergence zone and its multilevel flows. *Journal of the Atmospheric Sciences*,
692 **67** (12), 4028–4053.
- 693 Nolan, D. S., and E. D. Rappin, 2008: Increased sensitivity of tropical cyclogenesis to wind shear
694 in higher SST environments. *Geophysical Research Letters*, **35** (14).
- 695 Nolan, D. S., C. Zhang, and S.-h. Chen, 2007: Dynamics of the shallow meridional circulation
696 around intertropical convergence zones. *Journal of the Atmospheric Sciences*, **64** (7), 2262–
697 2285.
- 698 Pasch, R. J., and Coauthors, 2009: Eastern North Pacific hurricane season of 2006. *Monthly*
699 *Weather Review*, **137** (1), 3–20.
- 700 Petersen, W. A., R. Cifelli, D. J. Boccippio, S. A. Rutledge, and C. Fairall, 2003: Convection and
701 easterly wave structures observed in the eastern Pacific warm pool during EPIC-2001. *Journal*
702 *of the Atmospheric Sciences*, **60** (15), 1754–1773.

- 703 Poveda, G., L. Jaramillo, and L. F. Vallejo, 2014: Seasonal precipitation patterns along pathways
704 of South America low-level jets and aerial rivers. *Water Resources Research*, **50** (1), 98–118.
- 705 Rapp, A. D., A. G. Peterson, O. W. Frauenfeld, S. M. Quiring, and E. B. Roark, 2014: Climato-
706 logy of storm characteristics in Costa Rica using the TRMM precipitation radar. *Journal of*
707 *Hydrometeorology*, **15** (6), 2615–2633.
- 708 Rauber, R. M., S. M. Ellis, J. Vivekanandan, J. Stith, W.-C. Lee, G. M. McFarquhar, B. F. Jewett,
709 and A. Janiszewski, 2017: Finescale structure of a snowstorm over the northeastern United States:
710 A first look at high-resolution HIAPER cloud radar observations. *Bulletin of the American Me-*
711 *teorological Society*, **98** (2), 253–269.
- 712 Raymond, D. D., C. López-Carrillo, and L. L. Cavazos, 1998: Case-studies of developing east
713 Pacific easterly waves. *Quarterly Journal of the Royal Meteorological Society*, **124** (550), 2005–
714 2034.
- 715 Raymond, D. J., S. Gjorgjevska, S. Sessions, and Z. Fuchs, 2014: Tropical cyclogenesis and
716 mid-level vorticity. *Aust. Meteorol. Oceanogr. J.*, **64**, 11–25.
- 717 Reed, R. J., and R. H. Johnson, 1974: The vorticity budget of synoptic-scale wave disturbances in
718 the tropical western Pacific. *Journal of the Atmospheric Sciences*, **31** (7), 1784–1790.
- 719 Reed, R. J., D. C. Norquist, and E. E. Recker, 1977: The structure and properties of African wave
720 disturbances as observed during phase III of GATE. *Monthly Weather Review*, **105** (3), 317–333.
- 721 Reed, R. J., and E. E. Recker, 1971: Structure and properties of synoptic-scale wave disturbances
722 in the equatorial western Pacific. *Journal of the Atmospheric Sciences*, **28** (7), 1117–1133.
- 723 Rennick, M. A., 1976: The generation of African waves. *Journal of the Atmospheric Sciences*,
724 **33** (10), 1955–1969.

- 725 Riehl, H., 1954: Tropical meteorology. Tech. rep., McGraw-Hill.
- 726 Rydbeck, A. V., and E. D. Maloney, 2014: Energetics of east Pacific easterly waves during in-
727 traseasonal events. *Journal of Climate*, **27** (20), 7603–7621.
- 728 Rydbeck, A. V., and E. D. Maloney, 2015: On the convective coupling and moisture organization
729 of east Pacific easterly waves. *Journal of the Atmospheric Sciences*, **72** (10), 3850–3870.
- 730 Rydbeck, A. V., E. D. Maloney, and G. J. Alaka Jr, 2017: In situ initiation of east Pacific easterly
731 waves in a regional model. *Journal of the Atmospheric Sciences*, **74** (2), 333–351.
- 732 Schumacher, C., R. A. Houze Jr, and I. Kraucunas, 2004: The tropical dynamical response to
733 latent heating estimates derived from the TRMM precipitation radar. *Journal of the Atmospheric
734 Sciences*, **61** (12), 1341–1358.
- 735 Serra, Y. L., and R. A. Houze, 2002: Observations of variability on synoptic timescales in the east
736 Pacific ITCZ. *Journal of the Atmospheric Sciences*, **59** (10), 1723–1743.
- 737 Serra, Y. L., X. Jiang, B. Tian, J. Amador-Astua, E. D. Maloney, and G. N. Kiladis, 2014: Tropical
738 intraseasonal modes of the atmosphere. *Annual Review of Environment and Resources*, **39**, 189–
739 215.
- 740 Serra, Y. L., G. N. Kiladis, and M. F. Cronin, 2008: Horizontal and vertical structure of easterly
741 waves in the Pacific ITCZ. *Journal of the Atmospheric Sciences*, **65** (4), 1266–1284.
- 742 Serra, Y. L., G. N. Kiladis, and K. I. Hodges, 2010: Tracking and mean structure of easterly waves
743 over the Intra-Americas Sea. *Journal of Climate*, **23** (18), 4823–4840.
- 744 Shapiro, L. J., 1986: The three-dimensional structure of synoptic-scale disturbances over the trop-
745 ical Atlantic. *Monthly Weather Review*, **114** (10), 1876–1891.

- 746 Sherwood, S. C., P. Minnis, and M. McGill, 2004: Deep convective cloud-top heights and their
747 thermodynamic control during CRYSTAL-FACE. *Journal of Geophysical Research: Atmospheres*, **109** (D20).
- 748
- 749 Tai, K.-S., and Y. Ogura, 1987: An observational study of easterly waves over the eastern Pacific in
750 the northern summer using FGGE data. *Journal of the Atmospheric Sciences*, **44** (2), 339–361.
- 751
- 752 Thompson, R. M., S. W. Payne, E. E. Recker, and R. J. Reed, 1979: Structure and properties of
753 synoptic-scale wave disturbances in the intertropical convergence zone of the eastern Atlantic.
754 *Journal of the Atmospheric sciences*, **36** (1), 53–72.
- 755
- 756 Thorncroft, C., and B. Hoskins, 1994: An idealized study of African easterly waves. i: A linear
757 view. *Quarterly Journal of the Royal Meteorological Society*, **120** (518), 953–982.
- 758
- 759 Toma, V. E., and P. J. Webster, 2010a: Oscillations of the intertropical convergence zone and the
760 genesis of easterly waves. Part I: Diagnostics and theory. *Climate dynamics*, **34** (4), 587–604.
- 761
- 762 Toma, V. E., and P. J. Webster, 2010b: Oscillations of the Intertropical Convergence Zone and the
763 genesis of easterly waves Part II: numerical verification. *Climate dynamics*, **34** (4), 605–613.
- 764
- 765 Vömel, H., and Coauthors, 2020: High-resolution in situ observations of atmospheric thermody-
766 namics using dropsondes during the Organization of Tropical East Pacific Convection (OTREC)
767 field campaign. *Earth System Science Data Discussions*, 1–25.
- 768
- 769 Whitaker, J. W., and E. D. Maloney, 2018: Influence of the Madden-Julian Oscillation and
770 Caribbean low-level jet on east Pacific easterly wave dynamics. *Journal of the Atmospheric
771 Sciences*, **75** (4), 1121–1141.
- 772
- 773 Whitaker, J. W., and E. D. Maloney, 2020: Genesis of an east Pacific easterly wave from a Panama
774 Bight MCS: A case study analysis from June 2012. *Journal of the Atmospheric Sciences*, 1–50.
- 775

- 768 Wolding, B. O., E. D. Maloney, and M. Branson, 2016: Vertically resolved weak temperature gra-
769 dient analysis of the Madden-Julian Oscillation in SP-CESM. *Journal of Advances in Modeling*
770 *Earth Systems*, **8** (4), 1586–1619.
- 771 Xie, S.-P., H. Xu, W. S. Kessler, and M. Nonaka, 2005: Air-sea interaction over the eastern Pacific
772 warm pool: Gap winds, thermocline dome, and atmospheric convection. *Journal of Climate*,
773 **18** (1), 5–20.
- 774 Yokoyama, C., and Y. N. Takayabu, 2012: Relationships between rain characteristics and envi-
775 ronment. Part II: Atmospheric disturbances associated with shallow convection over the eastern
776 tropical Pacific. *Monthly Weather Review*, **140** (9), 2841–2859.
- 777 Zehnder, J. A., D. M. Powell, and D. L. Ropp, 1999: The interaction of easterly waves, orogra-
778 phy, and the intertropical convergence zone in the genesis of eastern Pacific tropical cyclones.
779 *Monthly Weather Review*, **127** (7), 1566–1585.
- 780 Zhang, C., M. McGauley, and N. A. Bond, 2004: Shallow meridional circulation in the tropical
781 eastern Pacific. *Journal of Climate*, **17** (1), 133–139.
- 782 Zhang, C., D. S. Nolan, C. D. Thorncroft, and H. Nguyen, 2008: Shallow meridional circulations
783 in the tropical atmosphere. *Journal of Climate*, **21** (14), 3453–3470.
- 784 Zuidema, P., B. Mapes, J. Lin, C. Fairall, and G. Wick, 2006: The interaction of clouds and dry
785 air in the eastern tropical Pacific. *Journal of Climate*, **19** (18), 4531–4544.

786 **LIST OF TABLES**

787 Table 1.	LCL (hPa), CAPE (J kg^{-1}), and CIN (J kg^{-1}) at 4°N and 8°N from the three	38
788 EWs at day +0 and +2 from OTREC RFs and ERA5	38	

789 TABLE 1. LCL (hPa), CAPE (J kg^{-1}), and CIN (J kg^{-1}) at 4°N and 8°N from the three EWs at day +0 and
 790 +2 from OTREC RFs and ERA5

EWs	Day 0					Day +2				
	Source (date)	Latitude	LCL	CAPE	CIN	Source (date)	Latitude	LCL	CAPE	CIN
EW 1	OTREC (Aug. 7)	8°N	971	1934	0	ERA5 (Aug. 9)	8°N	958	1713	0
		4°N	977	395	-68		4°N	954	276	-30
EW 2	ERA5 (Aug. 15)	8°N	968	1190	0	OTREC (Aug. 17)	8°N	975	2259	0
		4°N	958	207	-46		4°N	975	1053	-12
EW 3	ERA5 (Sep. 16)	8°N	974	1182	0	ERA5 (Sep. 18)	8N	956	1331	0
		4°N	972	62	-36		4°N	947	303	-44

791 **LIST OF FIGURES**

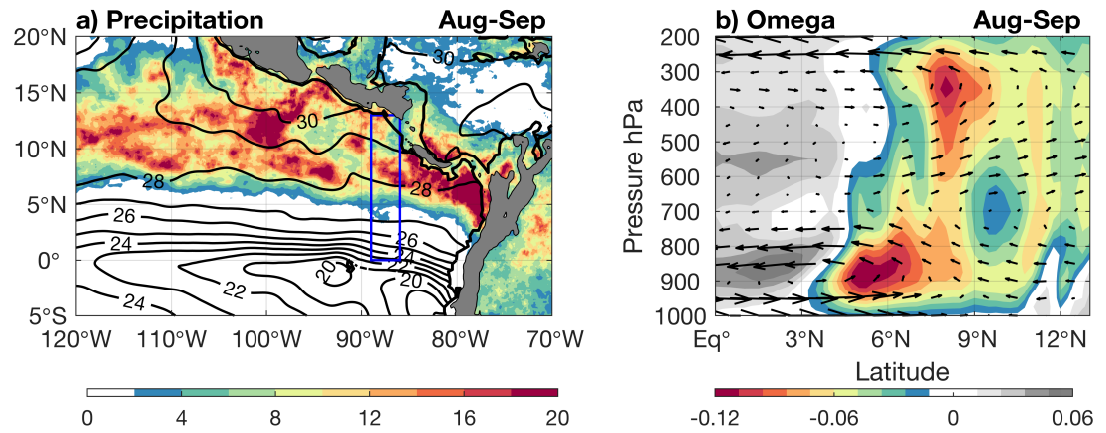
792 Fig. 1.	a) Total precipitation in mm d^{-1} from IMERG and SST in C° from OSTIA, and b) cross 793 section of omega in Pa s^{-1} and meridional flow across the OTREC region (blue rectangle in 794 a) from ERA5 for August and September 2019.	41
795 Fig. 2.	Hovmöller diagrams averaged from 3 - 11°N of a) precipitation in mm d^{-1} from IMERG, 796 and b) 600-hpa vorticity in s^{-1} and c) 600-hPa meridional winds in m s^{-1} from ERA5. Total 797 values are shaded and TD-band values are in contours (precipitation contours every 4 mm 798 d^{-1} , vorticity contours every 4 s^{-1} , and 600-hPa meridional wind contours every 2 m s^{-1}). 799 Symbols are placed in the OTREC region, the stars indicate OTREC RF dates and the circles 800 highlight enhanced convection (blue) and suppressed convection (red) associated with EWs.	42
801 Fig. 3.	Time series of total (left axis) and TD-band (right axis) IMERG precipitation over the East 802 Pacific OTREC flight box (89° - 86°W, 3° - 11°N). Dashed lines indicates the threshold of 803 TD-band precipitation over the OTREC period average ± 1.25 standard deviation. As in 804 Fig. 2, the stars indicate OTREC RFs and the circles highlight when EWs were present.	43
805 Fig. 4.	IMERG precipitation in mm d^{-1} averaged over the three OTREC EWs during a) enhanced 806 (day 0) and b) suppressed (day +2) conditions. Longitude-time diagrams of c) total pre- 807 cipitation and d) anomaly precipitation for the latitude range 3°-11°N during the three EW 808 events. The black box indicates the OTREC region box.	44
809 Fig. 5.	(a-c, g-i) Precipitation anomalies in mm d^{-1} superimposed with 600-hPa horizontal wind 810 anomalies across the East Pacific and (d-f, i-l) omega cross sections in Pa s^{-1} superposed 811 by meridional flow over the OTREC region (red rectangle) from day -2 to day +3 compos- 812 ited for the three EWs. The trough and ridge centers of the EW are labeled as T and R, 813 respectively. Largest wind vector is 5 m s^{-1}	45
814 Fig. 6.	Time-height diagrams of vorticity (s^{-1}), specific humidity (g kg^{-1}) , meridional wind (m 815 s^{-1}), and omega (Pa s^{-1}) anomalies at a-d) 7-11°N and e-h) 3-7°N averaged at 89-86°W 816 over the three OTREC EWs.	46
817 Fig. 7.	Skew-T diagrams for all the 3 EWs (08/07, 08/15 and 09/18) during the OTREC field cam- 818 paign from ERA5 and OTREC RFs at day 0 (left) and day 2 (right) for (a,b) 8°N and (c,d) 819 4°N. RF times are between 12-18 UTC.	47
820 Fig. 8.	(a-b, e-f) GOES IR images (red/dark colors indicate convective regions) and (c-d, g-h) verti- 821 cal reflectivity cross sections in dBZ from the NCAR Hiaper Cloud Radar during enhanced 822 precipitation on 7 August 2019 (i.e., positive phase of EW) and suppressed precipitation on 823 17 August 2019 (i.e., negative phase of EW) across the flight path indicated by the red arrow 824 in the GOES IR images. The trough and ridge centers of the EW are labeled as T and R, 825 respectively.	48
826 Fig. 9.	Composite OTREC EW anomalies (shaded, in mm d^{-1}) of (a-e) moisture tendency from 827 horizontal advection and (f-h) moisture tendency from vertical advection minus precipitation 828 from day -1 to day +3 using ERA5 reanalysis. All images are superposed by 600-hPa wind 829 vectors and ERA5 precipitation anomalies. Positive (negative) precipitation anomalies are 830 in blue (red) contours, contours are every 10 (5) mm d^{-1} starting at 5 mm d^{-1} . The trough 831 and ridge centers of the EW are labeled as T and R, respectively. Largest wind vector is 5 m 832 s^{-1}	49

- 833 **Fig. 10.** Composite OTREC EW time-latitude diagrams over 89° - 86° W of a-b) omega anomalies in
 834 Pa s^{-1} at 400 hPa and 900 hPa (dashed lines indicate the climatological position of
 835 maximum omega at the determined level), c-d) vertical and horizontal advection of total MSE in
 836 W m^{-2} , e) anomalies of moisture tendency from vertical advection in mm d^{-1} superposed
 837 by moisture tendency from vertical advection minus precipitation in mm d^{-1} (contours every
 838 2 mm d^{-1} , negative values dashed and positive values solid), and f) anomalies of moisture
 839 tendency from horizontal advection in mm d^{-1}

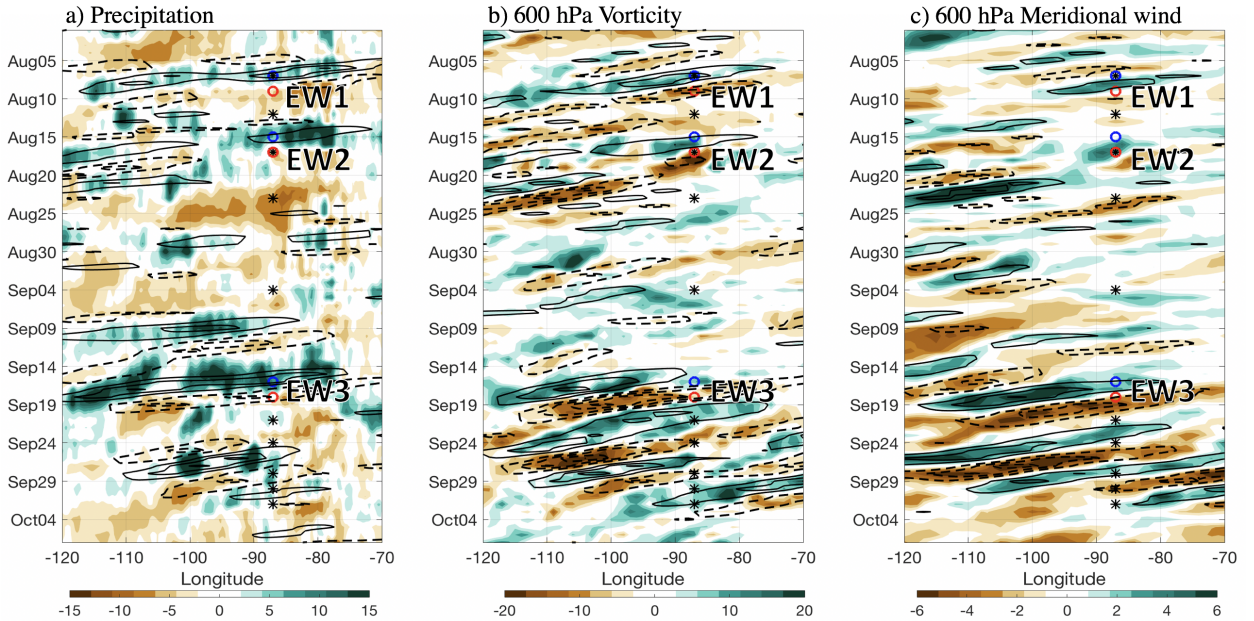
840 **Fig. 11.** Composite OTREC EW a-b) vertical velocity in Pa s^{-1} and meridional flow, c-d) relative
 841 humidity in % averaged over 89° - 86° W, and e-f) anomalies of moisture tendency from hor-
 842 izontal advection in shaded and vertical advection in contours superposed by winds at 850
 843 hPa during day 0 and +2. Positive (negative) vertical advection anomalies are in blue (red)
 844 contours, contours are every 5 mm d^{-1} starting at 3 mm d^{-1} . The trough and ridge centers
 845 of the EW are labeled as T and R, respectively. Largest wind vector is 6 m s^{-1}

846 **Fig. 12.** Meridional wind profiles from ERA5 in m s^{-1} at (a,b) 7 - 8° N, 89° - 86° W and (c, d) 4 -
 847 5° N, 89° - 86° W for the three EWs and the August-September average during day 0 (a, c)
 848 and +2 (b, d).

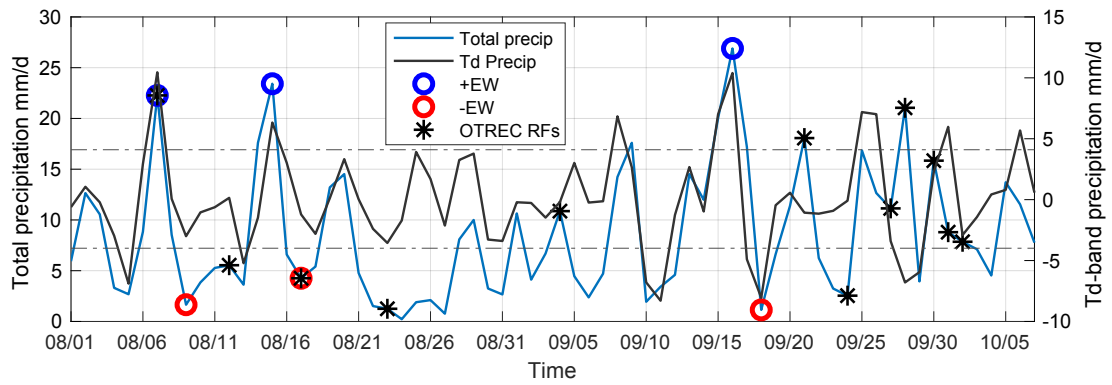
849 **Fig. 13.** Latitude-height sketch of the evolution of EWs and their effect on shallow and deep circu-
 850 lations in the East Pacific. Horizontal (vertical) bold vectors indicate total meridional winds
 851 (upward motion) larger than 8 m s^{-1} (0.3 Pa s^{-1}). Positive (negative) total vorticity is shown
 852 in a red cyclonic (blue anticyclonic) vertical vorticity features and bold trajectories indicate
 853 vorticity of magnitude larger than $4 \times 10^{-5} \text{ s}^{-1}$. The EW horizontal scale is approximated
 854 by the size of vorticity features. The clouds denote the position of the shallow and deep
 855 convection. Encircled x's (dots) denote westward (eastward) winds.



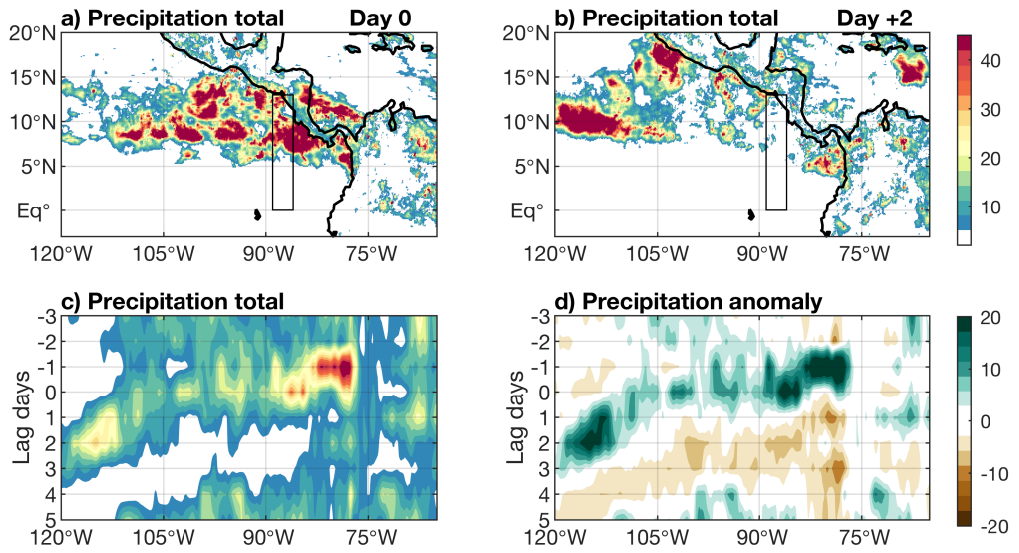
856 FIG. 1. a) Total precipitation in mm d^{-1} from IMERG and SST in C° from OSTIA, and b) cross section of
 857 omega in Pa s^{-1} and meridional flow across the OTREC region (blue rectangle in a) from ERA5 for August and
 858 September 2019.



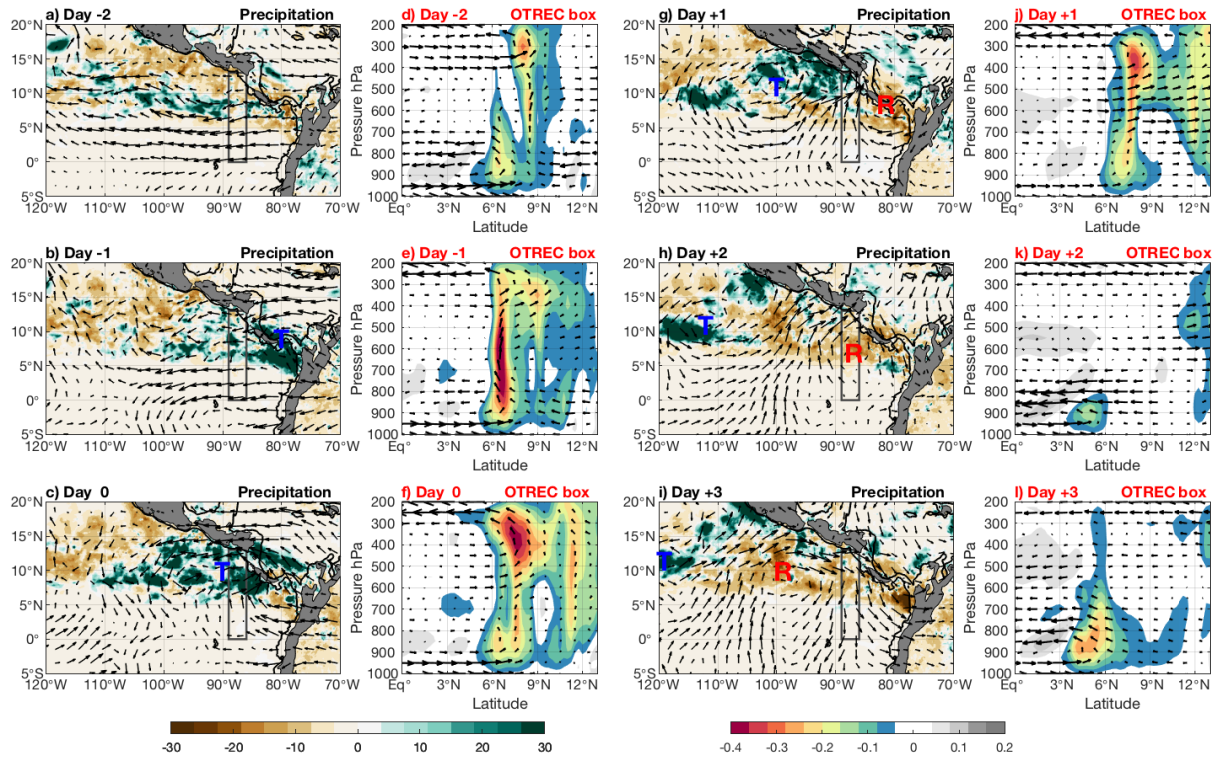
859 FIG. 2. Hovmöller diagrams averaged from $3 - 11^{\circ}\text{N}$ of a) precipitation in mm d^{-1} from IMERG, and b)
 860 600-hpa vorticity in s^{-1} and c) 600-hPa meridional winds in m s^{-1} from ERA5. Total values are shaded and TD-
 861 band values are in contours (precipitation contours every 4 mm d^{-1} , vorticity contours every 4 s^{-1} , and 600-hPa
 862 meridional wind contours every 2 m s^{-1}) . Symbols are placed in the OTREC region, the stars indicate OTREC
 863 RF dates and the circles highlight enhanced convection (blue) and suppressed convection (red) associated with
 864 EWs.



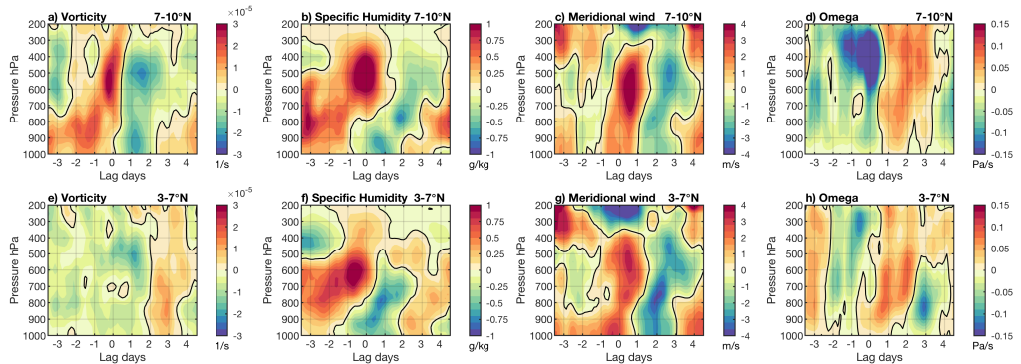
865 FIG. 3. Time series of total (left axis) and TD-band (right axis) IMERG precipitation over the East Pacific
 866 OTREC flight box (89° - 86° W, 3° - 11° N). Dashed lines indicates the threshold of TD-band precipitation over
 867 the OTREC period average ± 1.25 standard deviation. As in Fig. 2, the stars indicate OTREC RFs and the
 868 circles highlight when EWs were present.



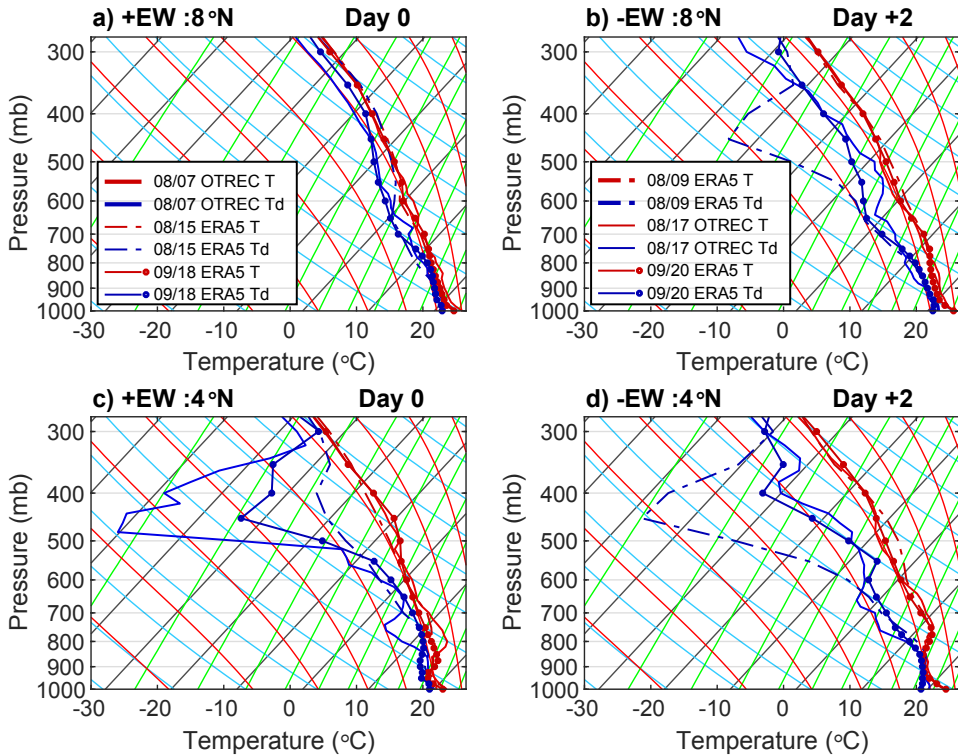
869 FIG. 4. IMERG precipitation in mm d^{-1} averaged over the three OTREC EWs during a) enhanced (day
 870 0) and b) suppressed (day +2) conditions. Longitude-time diagrams of c) total precipitation and d) anomaly
 871 precipitation for the latitude range 3° - 11° N during the three EW events. The black box indicates the OTREC
 872 region box.



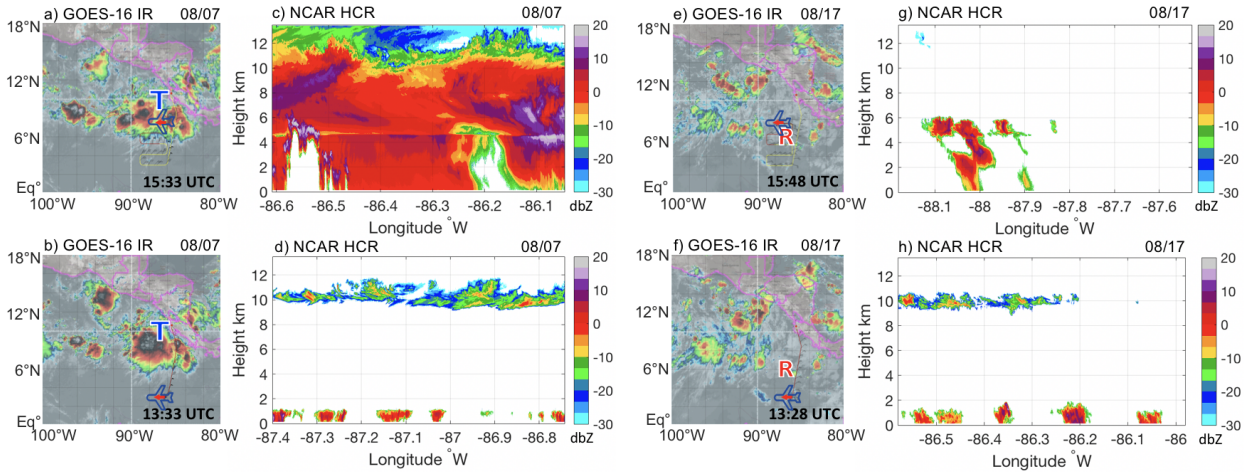
873 FIG. 5. (a-c, g-i) Precipitation anomalies in mm d^{-1} superimposed with 600-hPa horizontal wind anomalies
 874 across the East Pacific and (d-f, i-l) omega cross sections in Pa s^{-1} superposed by meridional flow over the
 875 OTREC region (red rectangle) from day -2 to day +3 composed for the three EWs. The trough and ridge
 876 centers of the EW are labeled as T and R, respectively. Largest wind vector is 5 m s^{-1} .



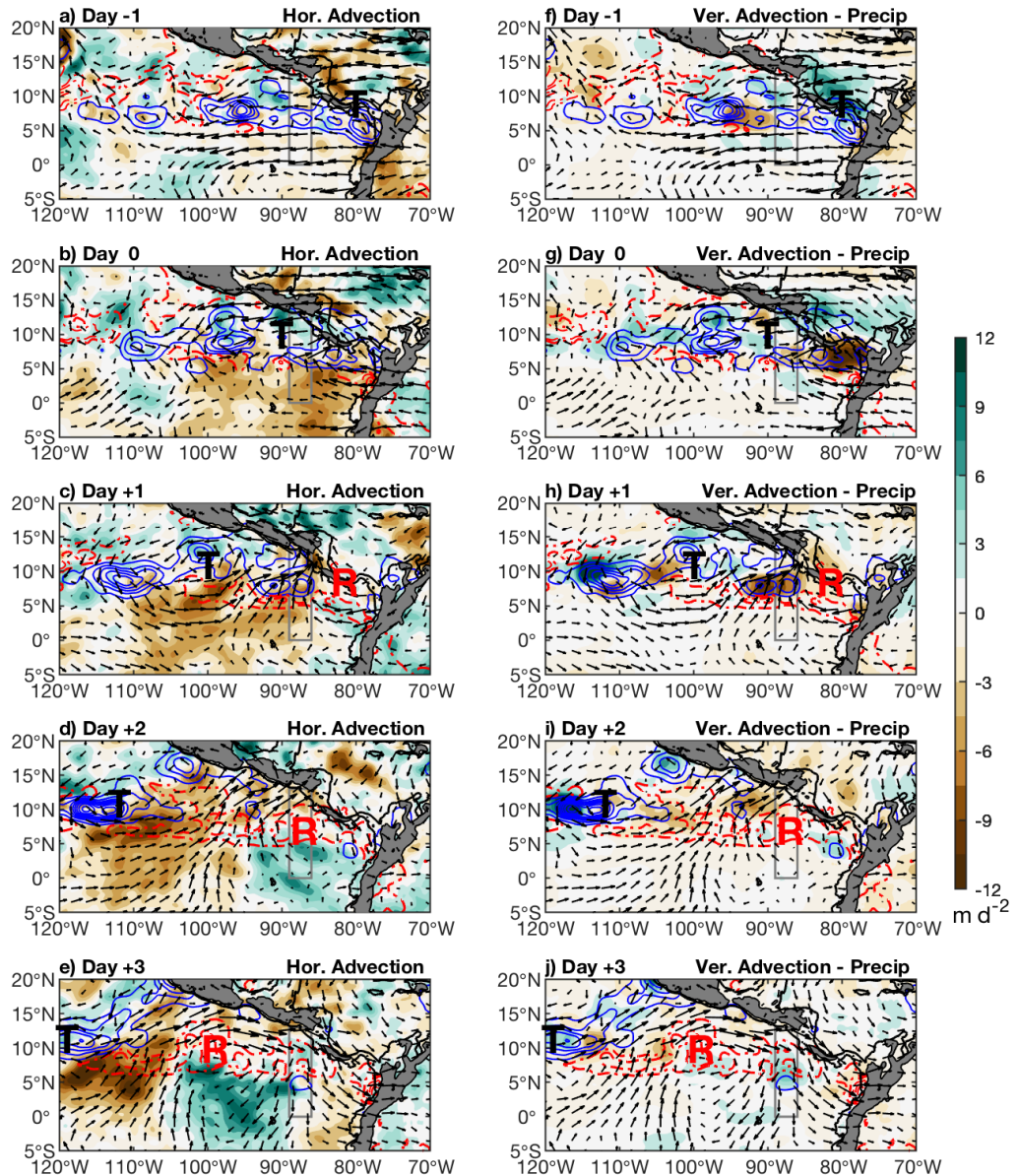
877 FIG. 6. Time-height diagrams of vorticity (s^{-1}), specific humidity (g kg^{-1}), meridional wind (m s^{-1}), and
878 omega (Pa s^{-1}) anomalies at a-d) 7-11°N and e-h) 3-7°N averaged at 89-86°W over the three OTREC EWs.



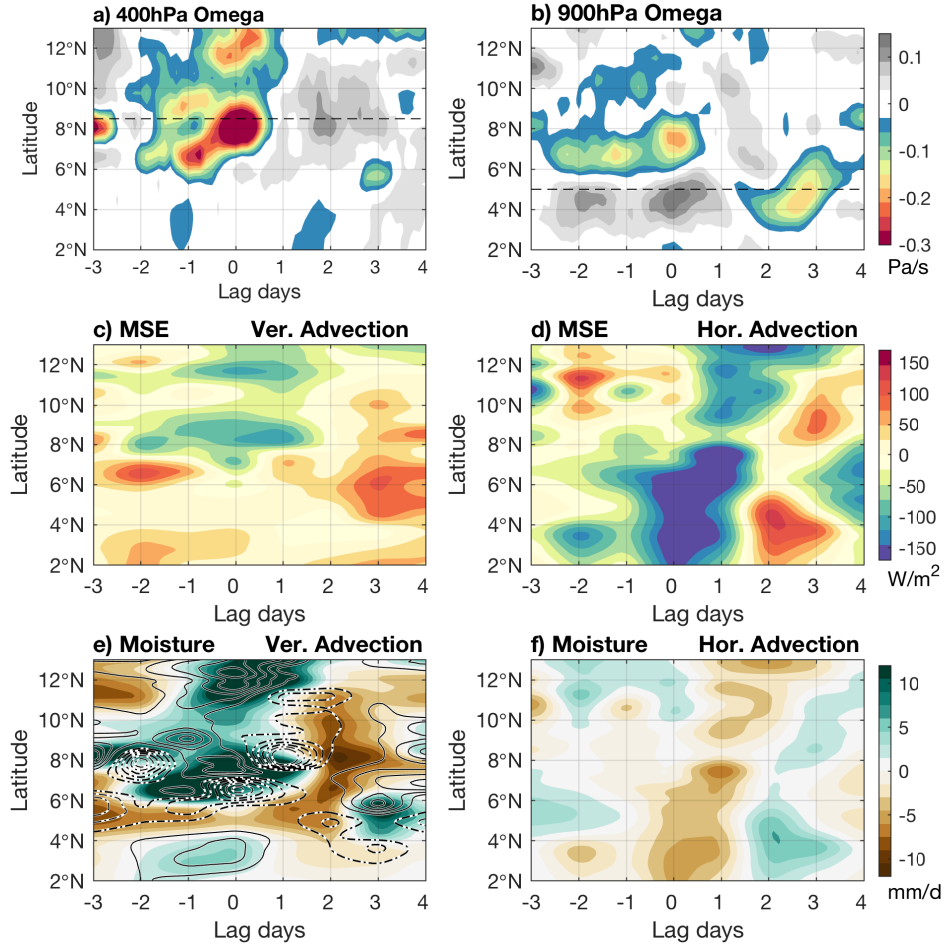
879 FIG. 7. Skew-T diagrams for all the 3 EWs (08/07, 08/15 and 09/18) during the OTREC field campaign from
 880 ERA5 and OTREC RFs at day 0 (left) and day 2 (right) for (a,b) 8°N and (c,d) 4°N. RF times are between 12-18
 881 UTC.



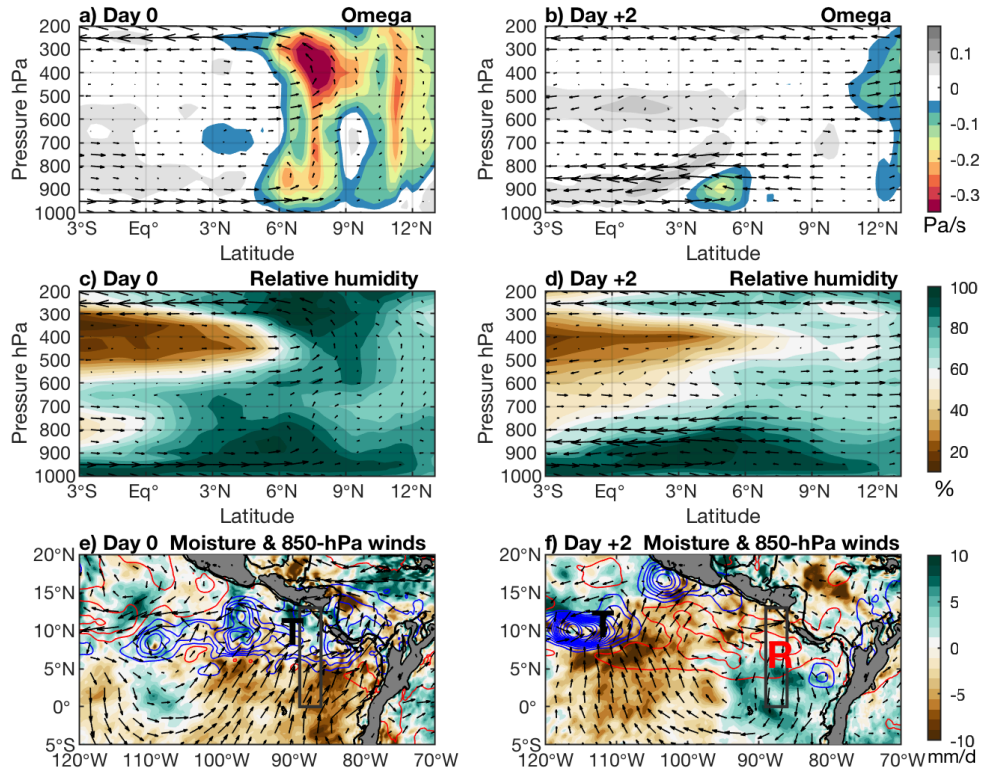
882 FIG. 8. (a-b, e-f) GOES IR images (red/dark colors indicate convective regions) and (c-d, g-h) vertical
 883 reflectivity cross sections in dBZ from the NCAR Hiaper Cloud Radar during enhanced precipitation on 7 August
 884 2019 (i.e., positive phase of EW) and suppressed precipitation on 17 August 2019 (i.e., negative phase of EW)
 885 across the flight path indicated by the red arrow in the GOES IR images. The trough and ridge centers of the
 886 EW are labeled as T and R, respectively.



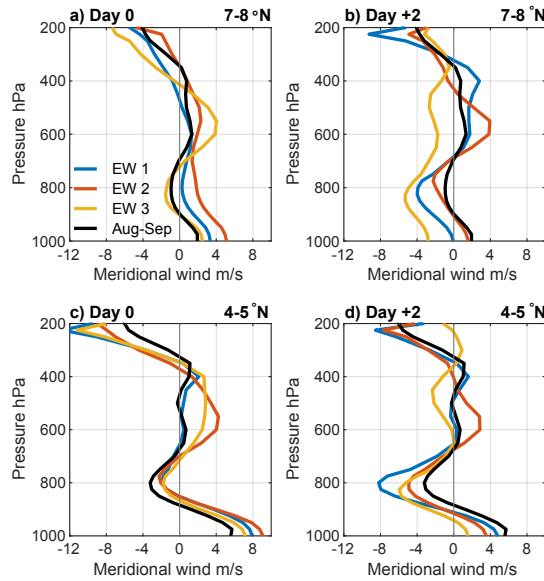
887 FIG. 9. Composite OTREC EW anomalies (shaded, in mm d^{-1}) of (a-e) moisture tendency from horizontal
 888 advection and (f-h) moisture tendency from vertical advection minus precipitation from day -1 to day +3 using
 889 ERA5 reanalysis. All images are superposed by 600-hPa wind vectors and ERA5 precipitation anomalies.
 890 Positive (negative) precipitation anomalies are in blue (red) contours, contours are every 10 (5) mm d^{-1} starting
 891 at 5 mm d^{-1} . The trough and ridge centers of the EW are labeled as T and R, respectively. Largest wind vector
 892 is 5 m s^{-1} .



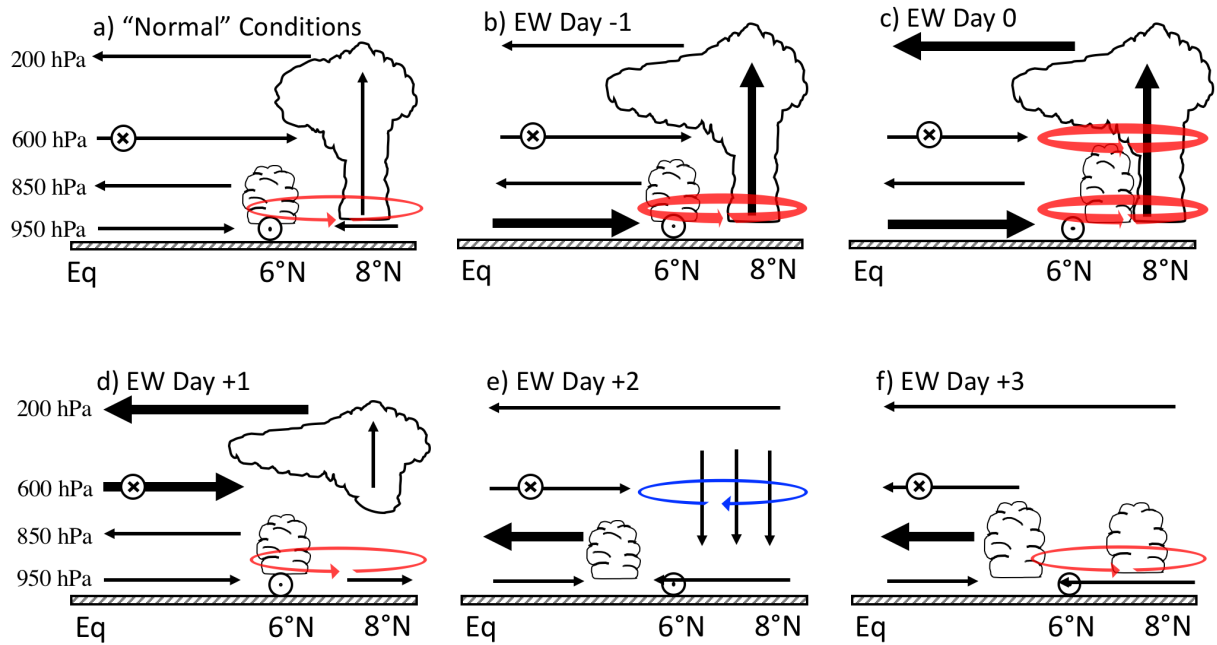
893 FIG. 10. Composite OTREC EW time-latitude diagrams over 89° - 86° W of a-b) omega anomalies in Pa s^{-1}
 894 at 400 hPa and 900 hPa (dashed lines indicate the climatological position of maximum omega at the determined
 895 level), c-d) vertical and horizontal advection of total MSE in W m^{-2} , e) anomalies of moisture tendency from
 896 vertical advection in mm d^{-1} superposed by moisture tendency from vertical advection minus precipitation in
 897 mm d^{-1} (contours every 2 mm d^{-1} , negative values dashed and positive values solid), and f) anomalies of
 898 moisture tendency from horizontal advection in mm d^{-1} .



899 FIG. 11. Composite OTREC EW a-b) vertical velocity in Pa s^{-1} and meridional flow, c-d) relative humidity
900 in % averaged over 89° - 86°W , and e-f) anomalies of moisture tendency from horizontal advection in shaded and
901 vertical advection in contours superposed by winds at 850 hPa during day 0 and +2. Positive (negative) vertical
902 advection anomalies are in blue (red) contours, contours are every 5 mm d^{-1} starting at 3 mm d^{-1} . The trough
903 and ridge centers of the EW are labeled as T and R, respectively. Largest wind vector is 6 m s^{-1} .



904 FIG. 12. Meridional wind profiles from ERA5 in m s^{-1} at (a,b) $7 - 8^\circ\text{N}$, $89^\circ - 86^\circ\text{W}$ and (c, d) $4 - 5^\circ\text{N}$, $89^\circ -$
 905 86°W for the three EWs and the August-September average during day 0 (a, c) and +2 (b, d).



906 FIG. 13. Latitude-height sketch of the evolution of EWs and their effect on shallow and deep circulations
 907 in the East Pacific. Horizontal (vertical) bold vectors indicate total meridional winds (upward motion) larger
 908 than 8 m s^{-1} (0.3 Pa s^{-1}). Positive (negative) total vorticity is shown in a red cyclonic (blue anticyclonic)
 909 vertical vorticity features and bold trajectories indicate vorticity of magnitude larger than $4 \times 10^{-5} \text{ s}^{-1}$. The EW
 910 horizontal scale is approximated by the size of vorticity features. The clouds denote the position of the shallow
 911 and deep convection . Encircled x's (dots) denote westward (eastward) winds.